The Astrophysical Journal, 646:143–160, 2006 July 20

THE TWO-DIMENSIONAL *XMM-NEWTON* GROUP SURVEY: $z < 0.012$ GROUPS

Alexis Finoguenov,[1,2] David S. Davis,[2,3] Marc Zimer,[1] and John S. Mulchaey[4]

Received 2004 July 1; accepted 2006 March 24

ABSTRACT

We present the results of the two-dimensional *XMM-Newton* Group Survey (2dXGS), an archival study of nearby galaxy groups. In this paper we consider 11 nearby systems ($z < 0.012$) in Mulchaey et al., which span a broad range in X-ray luminosity from 10^{40} to 10^{43} ergs s^{-1}. We measure the iron abundance and temperature distribution in these systems and derive pressure and entropy maps. We find statistically significant evidence for structure in the entropy and pressure of the gas component of seven groups on the 10%–20% level. The *XMM-Newton* data for the three groups with best statistics also suggest patchy metallicity distributions within the central 20–50 kpc of the brightest group galaxy, probed with 2–10 kpc resolution. This provides insights into the processes associated with thermalization of the stellar mass loss. Analysis of the global properties of the groups reveals a subclass of X-ray-faint groups, which are characterized by both higher entropy and lower pressure. We suggest that the merger history of the central elliptical is responsible for both the source and the observed thermodynamical properties of the hot gas of the X-ray-faint groups.

Subject headings: galaxies: clusters: general — intergalactic medium

Online material: color figures

1. INTRODUCTION

Groups of galaxies constitute the most common galaxy association, containing as much as 50%–70% of all galaxies in the nearby universe (Geller & Huchra 1983), and provide a link between the massive virialized systems such as clusters of galaxies and the field. For example, Finoguenov et al. (2003b) found that chemical enrichment in groups is very close to the prediction of the Salpeter initial mass function, known to characterize the star formation in the field. It was also suggested by Kodama et al. (2001) that properties of galaxies in clusters are largely defined by their previous group environment. Thus, studies of groups open prospects to understanding galaxy formation, at present one of the most challenging astrophysical issues.

Although the systems we study are defined by galaxy concentration, the presence of X-ray emission introduces further refinement in the definition and indicates that some of these systems are also *virialized* objects (Ostriker et al. 1995). Groups with a high fraction of early-type galaxies are more likely to exhibit detectable X-ray emission (Mulchaey et al. 1996). However, at low X-ray luminosities ($\sim 10^{41}$ ergs s^{-1}) the emission from individual galaxies becomes a nonnegligible contribution to the overall diffuse emission. Early-type galaxies show a wide range of X-ray properties, from "normal" emission to those early-type galaxies that have rather compact X-ray emission (Forman et al. 1985; Matsushita 2001; Finoguenov & Miniati 2004), while it has been suggested that others lack a massive dark matter halo (Romanowsky et al. 2003; but see Dekel et al. 2005). Group gas of bona fide collapsed halos, obeys well-defined X-ray scaling relations, and one can use these relationships to shed light on the large-scale dark matter distributions in these systems.

Comparative studies of the scaling relations in clusters of galaxies reveal strong deviations of the observed relations from predictions based on self-similar collapse (e.g., Ponman et al. 1996; Finoguenov et al. 2001). These deviations are thought to be best characterized by the injection of energy (preheating) into the gas before clusters collapse (Kaiser 1991; Evrard & Henry 1991). This entropy "floor" causes the simple self-similar scaling laws (Kaiser 1986) to predict a shallower L_X-T relationship. However, analysis of a large compilation of entropy profiles on groups and clusters of galaxies is inconsistent with this picture, requiring at r_{500} much larger entropy levels than were thought before (Finoguenov et al. 2002) and modifying the concept of the entropy floor to the entropy ramp at $0.1r_{200}$ (Ponman et al. 2003). Reproduction of these results, both analytically and numerically, strongly supports the scenario of Dos Santos & Doré (2002), in which an initial adiabatic state of the infalling gas is further modified by the accretion shock (Ponman et al. 2003; Voit et al. 2003; Voit & Ponman 2003; Borgani et al. 2005). As supporting evidence for the latter, Ponman et al. (2003) noticed a self-similarity in the entropy profiles, once scaled to $T^{0.65}$. Some *XMM-Newton* observations are consistent with this result (Pratt & Arnaud 2003; Finoguenov et al. 2004a, 2005). A major change introduced by these studies is that groups of galaxies can again be viewed as scaled-down versions of clusters, but with the scaling itself modified. Further evidence for the departure of groups from the trends seen in clusters has been recently refuted by Osmond & Ponman (2004).

In addition to preheating, internal heating by supernovae and active galactic nuclei (AGNs) may also impact the observed scaling relations. Recent results from *Chandra* demonstrate that AGN heating is likely very important in both the centers of clusters (McNamara et al. 2001) and early-type galaxies (Finoguenov & Jones 2001). However, very little work has been done to explore the role of AGN heating on the intragroup medium.

To better understand the physics of the intragroup medium, we have embarked on an *XMM-Newton* archival study of nearby

[1] Max-Planck-Institut für extraterrestrische Physik, Giessenbachstrasse, 85748 Garching, Germany; alexis@mpe.mpg.de, mzimer@mpe.mpg.de.

[2] Joint Center for Astrophysics and Physics Department, University of Maryland, Baltimore County, Baltimore, MD 21250.

[3] Laboratory for High Energy Astrophysics, NASA Goddard Space Flight Center, Code 661.0, Greenbelt, MD 20771; ddavis@milkyway.gsfc.nasa.gov.

[4] Observatories of the Carnegie Institution of Washington, 813 Santa Barbara Street, Pasadena, CA 91101; mulchaey@ociw.edu.

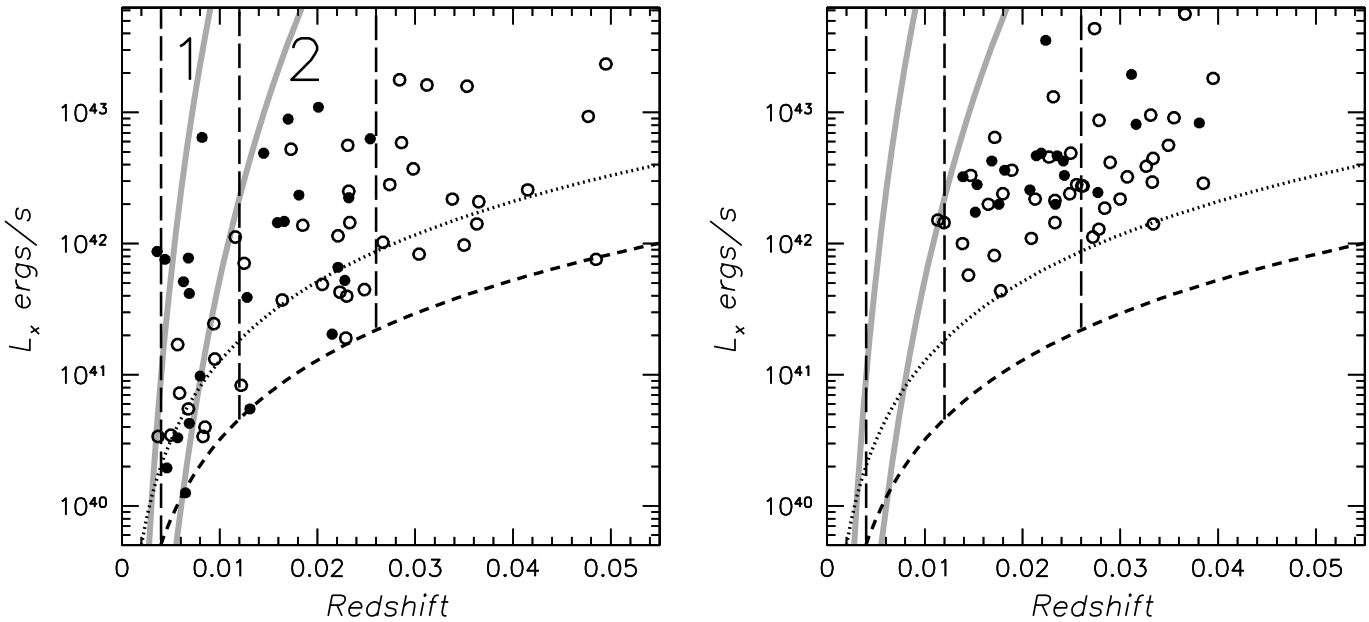

FIG. 1.—*Left*: Observed characteristics of the 2DXGS. The circles correspond to groups listed in Mulchaey et al. (2003). Filled circles denote objects observed by *XMM-Newton*. The change in the luminosity limit corresponding to the same X-ray flux in correspondence to Mulchaey and Mahdavi surveys is shown with short-dashed and dotted lines, respectively. The vertical long-dashed lines define the two subsamples in 2DXGS and are labeled "1" and "2." The analysis of the first subsample is reported here. The *XMM* FOV will enclose $\frac{1}{4}$ of the virial radius for the groups to the right of the low redshift gray line and $\frac{1}{2}$ of the virial radius for the higher redshift gray line. The quoted luminosities are bolometric assuming h_{100} (Mulchaey et al. 2003) and are measured out to the radius of X-ray detection. *Right*: Same as the left panel, but for the Mahdavi et al. (2000) group sample. The luminosities are given for 0.1–2.4 keV band, h_{100} and aperture of 500 kpc (Mahdavi et al. 2000). For systems in common with the Mulchaey et al. (2003) sample, these luminosities are lower by 0.1–0.2 dex, which is accounted for by the bolometric correction.

galaxy groups. The large field of view (FOV) of *XMM-Newton*, combined with its good resolution and large collecting area, make it an ideal instrument to study the hot gas in nearby groups. We also perform a study of how structure in the observed systems may affect their placement on the scaling relations for entropy. We adopt a Hubble constant of 70 km s^{-1} Mpc^{-1}, $\Omega_M = 1 - \Omega_\Lambda = 0.3$, and present redshifts corrected for the local motion.

2. SAMPLE SELECTION

At the moment there is no large purely X-ray-selected sample of groups of galaxies. For example, only a few objects, Fornax Cluster, MKW4, NGC 4636, NGC 1550, and NGC 5044, are present in the Highest X-Ray Flux Galaxy Cluster (HIFLUGS), a complete all-sky sample of brightest groups and clusters of galaxies (Reiprich & Böhringer 2002). Most present-day samples of groups are based on the X-ray follow-up of optical surveys (e.g., Mahdavi et al. 2000; Mulchaey et al. 2003).

For this study we have selected the groups in Mulchaey et al. (2003) with publicly available *XMM-Newton* (Jansen et al. 2001) observations. Most of the groups in the Mulchaey et al. (2003) sample were found by cross-correlating the *ROSAT* observation log with the positions of optically selected groups in the catalogs of Hickson (1982), Huchra & Geller (1982), Geller & Huchra (1983), Maia et al. (1989), Nolthenius (1993), and Garcia (1993). In addition to the optically selected groups, the Mulchaey et al. (2003) sample includes a small number of groups that were discovered in the *ROSAT* All-Sky Survey (RASS). Their final group list contains 109 systems.

The properties of groups from the Mulchaey et al. (2003) sample are shown in Figure 1. The flux limit corresponds to 2.6×10^{-13} ergs s^{-1} cm^{-2} at a 3 σ detection level, which is a factor of 4 lower than the flux limit in the Mahdavi et al. (2000) sample, a factor of 10 lower than in the REFLEX/NORAS surveys and a factor of 100 lower compared to HIFLUGS (these latter surveys are all based on the RASS data). The distribution of systems in Figure 1 is quite homogeneous, as are the targets observed by *XMM-Newton* (which covers 50% of groups at redshifts lower than 0.025; independent of the volume and luminosity cut). By construction, the Mulchaey et al. (2003) group list covers a fraction of a percent of the sky for serendipitous systems, yet it includes a larger fraction of bright objects, that were selected as primary targets for *ROSAT* pointings, e.g., three of the four HIFLUGS groups are included.

As we are interested in studying the spatial variations in the intragroup medium, we limit our analysis here to nearby groups. However, for the very nearest groups in the Mulchaey et al. (2003) sample, only the very centers of the group are covered in a single *XMM-Newton* pointing. Thus, we restrict our sample to the redshift bin 0.004–0.012. Results for the higher redshift bin 0.012–0.025 are presented in Finoguenov et al. (2006). In addition, eight groups from the Mahdavi sample are analyzed in Mahdavi et al. (2005). Two of the *XMM-Newton* targets in our redshift bin had no diffuse emission detection with *ROSAT* (NGC 4168 and NGC 7582), but we include them here for completeness.

The basic properties of our sample groups are listed in Table 1. Column (1) gives the name of the group, column (2) the velocity dispersion of the group, column (3) the number of galaxies identified with the group, columns (4)–(6) the properties of the central galaxy: effective radius, blue luminosity and central velocity dispersion, column (7) X-ray luminosity scaled to h_{70}^{-2} as tabulated in Mulchaey et al. (2003), column (8) redshift, and column (9) r_{500} in kpc, calculated as $r_{500} = 0.391$ Mpc $\times (kT/\mathrm{keV})^{0.63}\ h_{70}^{-1}$ using the M-T relation (F. Pacaud 2005, private communication) rederived from Finoguenov et al. (2001) using an orthogonal regression and correcting the masses to h_{70} and a ΛCDM cosmology. The optical data are collected from Bender et al. (1992), Koprolin & Zeilinger (2000), and Davies et al. (1987). NGC 3665 and NGC 2300 are classified as S0 and

TABLE 1
Basic Properties of the Sample

Name (1)	σ_{gr} (km s^{-1}) (2)	N_{gr} (3)	r_e (kpc) (4)	log $L_{B,\odot}$ (5)	σ_c (km s^{-1}) (6)	log L_X (ergs s^{-1}) (7)	z_{BCG} (10^{-4}) (8)	r_{500} (kpc) (9)
NGC 2300	278^{+35}_{-31}	16		10.41	254 ± 23	41.93 ± 0.04	65	339
NGC 3665	45^{+48}_{-44}	6		10.70	186 ± 11	40.94 ± 0.37	69	222
IC 1459	256^{+44}_{-38}	11	4.4	10.37	308 ± 7	40.83 ± 0.36	56	280
NGC 3923	191^{+126}_{-115}	9	13.	10.52	275 ± 23	40.60 ± 0.37	58	280
NGC 4168	259^{+56}_{-52}	10	6.9	10.40	182 ± 11	<40.87	76	258
NGC 4261	429^{+54}_{-50}	43	5.5	10.70	294 ± 16	42.20 ± 0.07	75	451
NGC 4636	n/a	1	7.1	10.51	191 ± 12	42.19 ± 0.20	31	331
NGC 5044	357^{+48}_{-42}	15	19.	10.70	238 ± 2	43.12 ± 0.02	90	430
NGC 5322	198^{+124}_{-117}	7	5.2	10.67	224 ± 5	40.41 ± 0.38	59	283
NGC 5846	368^{+51}_{-46}	20	9.2	10.66	278 ± 23	42.02 ± 0.17	57	309
NGC 7582	38^{+37}_{-36}	8				<41.05	54	

NGC 7582 is classified as a spiral (de Vaucouleurs et al. 1991; hereafter RC3). After a careful investigation, we could not confirm the members of the NGC 4636 group (see § 5.7).

3. DATA ANALYSIS

Table 2 lists details of the observations. Column (1) lists the name of the group; column (2) is the assigned *XMM-Newton* archival name; column (3) is the net Epic-pn exposure after removal of flaring episodes; column (4) lists the pn filter used, which determines the choice of instrumental response as well as background estimates, column (5) the *XMM-Newton* revolution number, which is useful to assess any secular evolution of the instrumental background, and column (6) the pn frame time, which is used to determine the fraction of out-of-time events (OOTEs).

The initial steps of the data reduction are similar to that described in Zhang et al. (2004) and Finoguenov et al. (2003a). One important aspect of the data preparation is to remove flares, which can significantly enhance the detector background and severely limit the detection of low surface brightness features. Thus, for the group analysis, using flare-free periods is critical. To identify time intervals with flares we look at energies above 10 keV at which telescope efficiency is quite low and the particle background dominates the source counts. We use the 10–15 keV energy band (binned in 100 s intervals) to monitor the particle background and to excise periods of high particle flux. In this screening process we use the events with `FLAG=0` and `PATTERN<5(13)` for the pn (MOS) data. We reject time intervals affected by flares by excising periods in which the detector count rate exceeds 2 σ above the mean quiescent rate.

Since most of the observations analyzed here were performed using a short integration frame time for pn, it is important to remove the OOTEs for accurate imaging and spectral analysis. We used the standard product of the `epchain` Science Analysis Software (SAS; XMMSAS 6.1) task to produce the simulated OOTE file for all the observations and scaled it by the fraction of the OOTE expected for the frame exposure time, as specified in Table 2.

For the broadband analysis we have used both pn and MOS data, while in the spectral analysis we only use pn data in order to take advantage of our expertise on the background subtraction for pn. In addition, the pn spectra have the highest statistics for the groups. We use response matrices released under XMMSAS 6.1.[5]

Analysis of the groups consists of two main steps: estimating the temperature structure of groups and verifying the structure using spectral analysis. Only the results of the spectral analysis are used in tabulations and comparison studies. The initial maps based on the hardness ratios are only used to locate the substructure. Quantitative analysis of the substructure, possible only for a subsample of systems is based on the spectral analysis.[6]

[5] For further details of *XMM-Newton* processing we refer the reader to http://wave.xray.mpe.mpg.de/xmm/cookbook/general.

[6] The two-dimensional information, related to the analysis reported in this paper, is released at http://www.mpe.mpg.de/2dXGS.

TABLE 2
Log of the *XMM-Newton* Epic-pn Observations of Groups

Name (1)	ObsID (2)	Net Exposure (ks) (3)	pn Filter (4)	*XMM* Orbit (5)	Frame Time (ms) (6)
NGC 2300	0022340201	42.3	Thin	232	73
NGC 3665	0052140201	19.5	Medium	363	199
IC 1459	0135980201	26.3	Medium	438	73
NGC 3923	0027340101	30.3	Thin	379	73
NGC 4168	0112550501	15.8	Medium	364	199
NGC 4261	0056340101	20.3	Medium	370	73
NGC 4636	0111190701	55.7	Medium	197	73
NGC 5044	0037950101	10.5	Medium	201	73
NGC 5322	0071340501	13.6	Thin	374	73
NGC 5846	0021540101	28.6	Thin	207	73
NGC 7582	0112310201	17.8	Medium	267	73

The first part of the analysis consists of producing temperature estimates for each of the systems. We use the surface brightness in conjunction with the hardness ratio maps to locate regions of similar intensity and color. The input data are based on images corrected for the instrumental effects discussed above and are background subtracted. The surface brightness is a wavelet-reconstructed (Vikhlinin et al. 1998) image in the 0.5–2 keV band and the hardness of the emission is a ratio of the wavelet-reconstructed images in the 0.5–1 and 1–2 keV bands. An advantage of using wavelets is the ability to remove additional background by spatial filtering, as well as control over the statistical significance of the detected structure. We apply a 4 σ detection threshold, followed out to a 90% confidence limit, a trous method of wavelet image reconstruction with scales from 8″ to 4′. Complications arise since the wavelet algorithm splits the image into discrete scales, resulting in small-scale discontinuities in the reconstructed image, which we overcome by applying additional smoothing before producing the hardness ratio map. The point sources are not removed in the imaging analysis.

We also construct pseudo-entropy and pressure maps using the image and the hardness ratio map. Although these maps suffer from a number of degeneracies, with metallicity-density being the strongest, since a significant fraction of the group X-ray emission is due to lines, they indicate the regions of primary interest for the detailed spectroscopic analysis that allows most of the degeneracies to be resolved. For a system in hydrostatic equilibrium, we expect the entropy to monotonically increase with the increasing radius (e.g., Metzler & Evrard 1994), while the pressure should decrease with radius.

The spectroscopic part of the analysis uses a mask file. This mask is created using the results of the hardness ratio and surface brightness analysis described above. The first application of this technique is presented in Finoguenov et al. (2004b). In our analysis we wish to select contiguous regions with similar spectral properties. This allows us to combine regions so that counting statistics are not the limiting factor in our derivation of the group properties. To select regions we use the wavelet-based hardness ratio maps to identify regions with similar X-ray colors and similar intensity level. To generate the mask file for use in further spectral analysis we use hardness ratios that correspond to temperatures in the ranges 0.48–0.56–0.60–0.64–0.72–0.8–0.9–1.0–1.1–1.2 keV and have intensities that are the same within a factor of 2. We then examine each of the isolated regions with approximately equal color and intensity imposing the additional criterion that the regions should be larger than the point-spread function (PSF; 15″) width and contain more than 300 counts in the raw pn image.

To demonstrate the performance of the technique, for NGC 4636 we compare the temperatures obtained in the spectral analysis with the temperatures estimated from the hardness ratio map within the central 5′ radius (Fig. 2). The mask file is used to extract the spectra and to estimated the mean and dispersion of the expected temperature from the hardness ratio map. The values from the spectral analysis are taken as the best-fit values, and we use the corresponding 68% confidence interval. We find that the estimated and measured temperatures agree to within 20%. The spectral and hardness ratio temperatures show a systematic offset below about 0.85 keV, with the hardness ratio temperatures being ~20% cooler than the fitted temperatures. The scatter about the best-fit line is less than ~10%, which matches our errors in determining the temperature. This shows that the hardness ratio in the 0.5–1 to 1–2 keV bands reflect the temperature of the gas. The cause of systematic deviations from unity is likely due to the higher absorption column assumed in determining the hardness ratio to temperature conversion. The systematic offset between the hardness ratio temperature and the spectral temperature is such that it could result from uncertainties in the Fe abundance. The tabulated results are from the spectral fits and the column density and abundance are fitted.

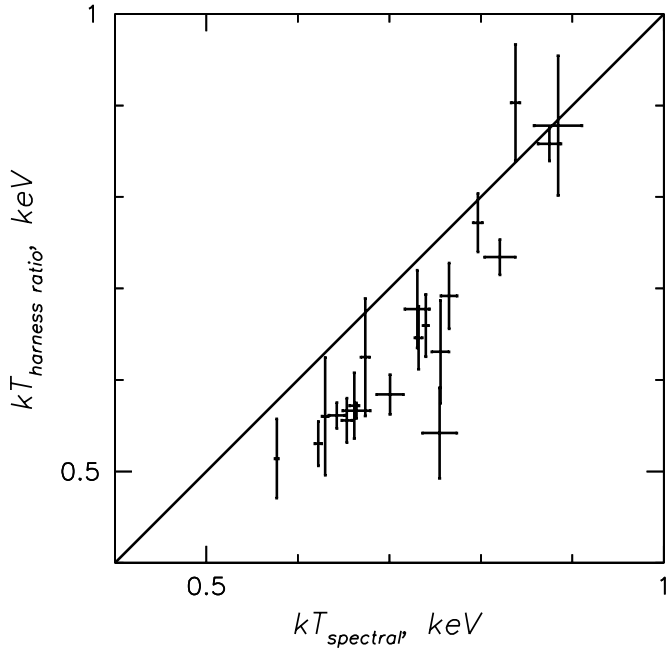

Fig. 2.—Comparison between the temperature derived from the spectral analysis and the temperature estimated from the hardness ratio in NGC 4636.

The spectral analysis was performed using the single-temperature APEC plasma code, fitting the abundance of O–Ni as one group with their relative abundances at the photospheric solar abundance ratios of Anders & Grevesse (1989). Absorption was fixed at the Galactic value, reported in Table 3.

In the spectral analysis, special attention was paid to the issue of the background estimation. We employ a double-subtraction technique, following Zhang et al. (2004). We used the 12′–16′ radius and 2–12 keV band to estimate the quality of the background subtraction using the blank fields. Variations in the background are found on the 20% level, in agreement with other studies (Freyberg et al. 2004). In our analysis of groups, we fix the shape of the background component and add a 0.2 keV thermal (APEC with solar element abundance) component to account for a possible variation in the Galactic foreground, allowing the normalizations of both components to be fit. Better estimation of the background allows one to carry out the spectral analysis throughout the detector if emission is found or set strict upper limits otherwise. Typically, an improvement of χ^2 is achieved for luminous parts of the group.

The metal abundance for the plasma model was explored using three approaches: element abundance fixed at 0.3 solar value, variable element abundance, variable abundance plus a 1.5 slope power-law component to account for the contribution of low-mass X-ray binaries (LMXBs). We use 0.4–5 keV band for fitting and group the channels to achieve 30 counts per bin to use the χ^2 statistic. In two cases (IC 1459, NGC 4261) an additional component was added to fit the contribution of the AGN in the center of the group. All other identified point sources were excised from the spectral extraction. Some regions, which had too few counts for spectral analysis and could not be combined with other regions on the basis of color or intensity, are not analyzed and appear as excised sources. The results obtained with the fixed

TABLE 3
PROPERTIES OF GROUPS WITHIN CENTRAL 30 h_{70}^{-1} kpc

Name (1)	N_H (10^{20} cm^{-2}) (2)	D_L (Mpc) (3)	Arcminute (kpc) (4)	kT (keV) (5)	Z ($Z_\odot$) (6)	L_X (10^{41} ergs s^{-1}) (7)
NGC 2300	5.27	28.0	8.05	0.79 ± 0.01	0.40 ± 0.04	1.03
NGC 3665	2.06	29.8	8.54	0.40 ± 0.02	0.25 ± 0.08	0.29
IC 1459	1.18	24.2	6.94	0.59 ± 0.01	0.46 ± 0.14	0.53
NGC 3923	6.21	25.0	7.19	0.57 ± 0.01	0.20 ± 0.01	1.32
NGC 4168	2.56	32.8	9.40	0.76 ± 0.05	0.08 ± 0.03	0.19
NGC 4261	1.55	32.4	9.28	1.24 ± 0.03	0.33 ± 0.04	0.63
NGC 4636	1.81	13.3	3.86	0.69 ± 0.01	0.51 ± 0.01	8.14
NGC 5044	4.93	38.9	11.1	0.90 ± 0.01	0.56 ± 0.01	28.0
NGC 5322	1.81	25.4	7.31	0.30 ± 0.01	0.09 ± 0.03	0.08
NGC 5846	4.26	24.6	7.07	0.70 ± 0.01	0.45 ± 0.01	3.05

element abundance are only used to evaluate the temperature structure when statistics are poor. Results from these fits are not used to derive any of the quantities given in the tables.

To estimate the pressure and entropy in each region, we need to estimate the length of the column for each selected two-dimensional region on the sky. We assume a geometry in which every region is a part of a spherical shell that is centered on the system core and has its inner and outer radii passing through the nearest and furthest points of the selected region, respectively. This spherical shell is further intersected by a cylinder that is directed toward the observer and has the cross-section of the selected region in the observer plane. For the concentric regions our geometry corresponds to a usual "onion-peeling" technique (e.g., Finoguenov & Ponman 1999). We assume a constant gas distribution with the integrated emissivity in the region matched to the measured emissivity in the spectral analysis. With these approximations the longest length through each volume is $L = 2(r_{\rm max}^2 - r_{\rm min}^2)^{1/2}$. The volume of the region is then $\frac{2}{3}SL$, where S is the area of the region. For reasonable assumptions of the geometry, the systematic uncertainty introduced by the volume estimate is 5%. Further details can be found in Henry et al. (2004) and Mahdavi et al. (2005). We also analyzed regions using concentric annuli. The data for the annuli are extracted after excising point sources, as well as the diffuse background sources identified in the text (NGC 4168) and the substructure exceeding 50% (important for NGC 2300, NGC 5322, and NGC 4636) of the expected value. The annular analysis is used mainly to sample the outermost regions, as well as to provide a comparison with the standard technique of volume estimate.

4. DISCUSSION and RESULTS

Early examples of two-dimensional studies of groups were carried out using *ROSAT* Position Sensitive Proportional Counter (PSPC) observations, which provided a reasonable sensitivity to both the group temperature and group luminosity. Some of these include M86 (e.g., Finoguenov & Jones 2000), NGC 2300 (Mulchaey et al. 1993; Davis et al. 1996), NGC 4261 (Davis et al. 1996), NGC 4636 (Trinchieri et al. 1994), NGC 5044 (David et al. 1994), and NGC 5846 (Finoguenov et al. 1999). For a more complete review we refer the reader to Mulchaey (2000). The *XMM-Newton* data cover a different spatial scale, different energy range, and the PSF is much different than that used in the earlier *ROSAT* analysis. Thus, a comparison of our results to those in the literature helps to determine how the derived X-ray characteristics of the groups are affected by the characteristics of different instruments.

4.1. *Global Properties*

Before proceeding with describing the structure of the systems in our study, in this section we provide an overview on the global properties of the groups. This is done in several different ways. A traditional comparison is presented in Table 3, where we estimate the temperature, luminosity, and element abundance from a single spectrum, extracted using a circular region with a radius of 30 kpc. In Tables 3–5 we list the properties of the gas within various fractions of r_{500}. In Figure 3 we present the entropy and pressure profiles derived using the extracted spectra and compare them with the known scaling relations. We show both the values derived using annuli, where we excise the zones associated with galaxies other then the central galaxies and deviations exceeding 30% (e.g., a background galaxy in NGC 4168; a spiral galaxy in NGC 2300; a tail in NGC 4636), and the values determined using the maps, plotting the corresponding values versus their distance from the group's center. The latter comparison is the most sophisticated and provides considerably more insight into the state of the gas than the more traditional approaches. We have divided the sample into two groups for presentation (Fig. 3). While we provide a careful discussion of the trends below, one can already see some drastic differences in both entropy and pressure between the groups NGC 5044, NGC 5846, and NGC 4636 and the rest of the sample. For comparison, In Figure 3 we also show the typical entropy and pressure profiles as observed by *XMM-Newton* in galaxy groups of bolometric luminosity well in excess of 10^{42} ergs s^{-1} (Finoguenov et al. 2006).

We have compared the global properties of the groups analyzed here with the Epic-pn camera and the global properties of these groups in the literature. Complicating this comparison is that we have included the central group galaxy in our global properties, and we have not matched our extraction radii to other studies. Despite this fact, we find an agreement within the statistical errors between our global temperatures and the *ROSAT* measurements given in Mulchaey et al. (2003) for groups with temperatures below 1 keV. There are two groups above 1 keV in our sample and the *XMM-Newton* results show that these groups have 20% higher temperatures than reported in the literature. A similar trend has been noted for groups studied with ASCA (Hwang et al. 1999; Mulchaey et al. 2003). One of these groups, NGC 5044, has been analyzed in detail by Finoguenov & Ponman (1999), and a comparison of the temperature profile has been made using the *Advanced Satellite for Cosmology and Astrophysics* (*ASCA*) and *ROSAT* data. This analysis shows that the data agree outside the central 30 h_{70}^{-1} kpc. This possibly indicates an

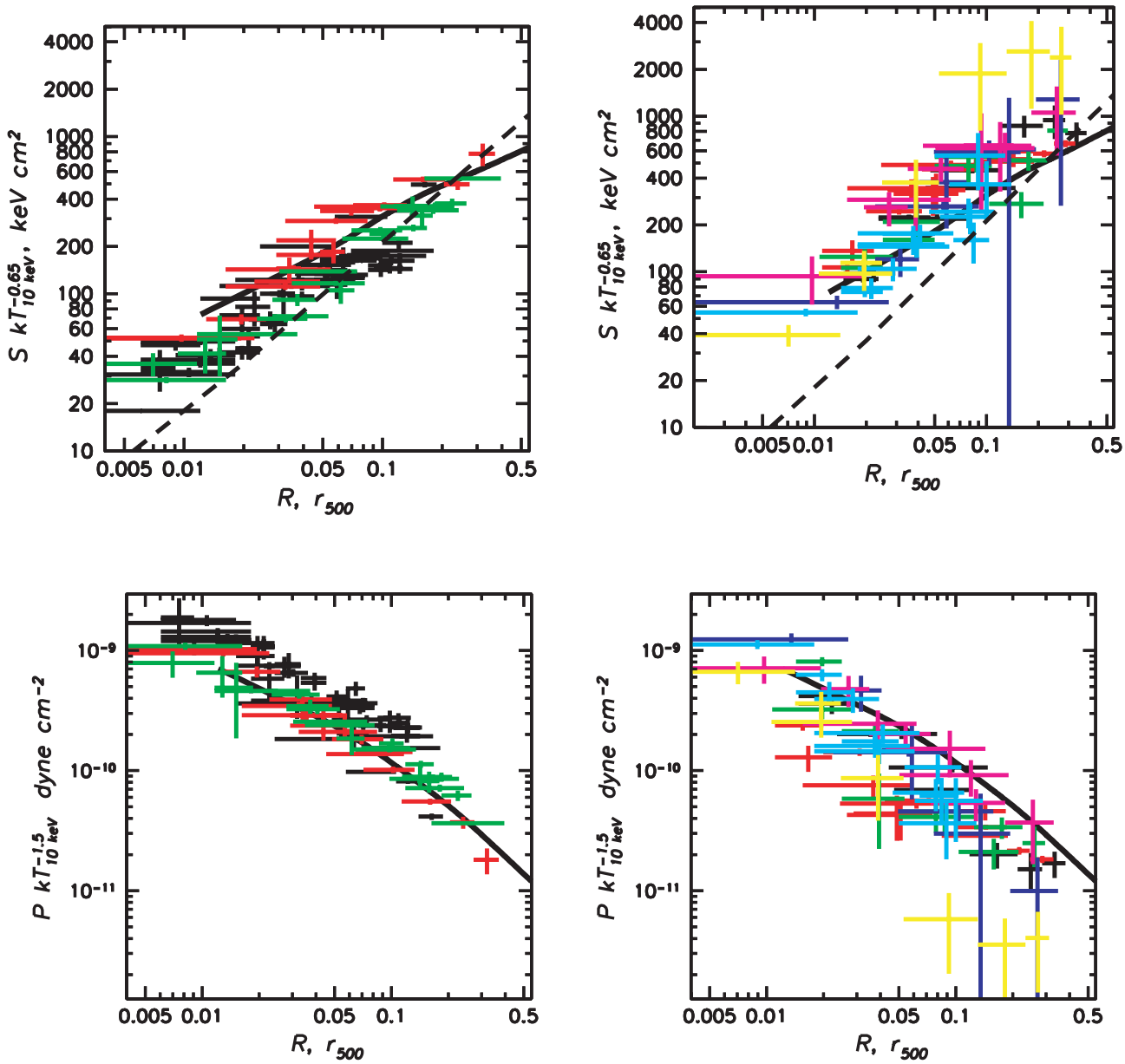

FIG. 3.—Scaled entropy (*top*) and pressure (*bottom*) profiles for the sample, obtained from spectral analysis. *Left*: NGC 4636 (*black*), NGC 5846 (*red*), NGC 5044 (*green*). *Right*: NGC 2300 (*black*), NGC 4261 (*red*), IC 1459 (*green*), NGC 3665 (*blue*), NGC 4168 (*magenta*), NGC 3923 (*cyan*), and NGC 5322 (*yellow*). The scaling for entropy and pressure is done in accordance with the results of Ponman et al. (2003). The dashed line on both entropy panels shows the $r^{1.1}$ law, expected in theory. The solid lines on each panel represents the typical profiles of X-ray luminous groups from Finoguenov et al. (2006) from two other samples shown in Fig. 1.

importance of low-temperature components in defining the mean temperatures obtained with the *ROSAT* PSPC. Our temperature value of 1.21 ± 0.01 keV for NGC 5044, obtained within the range 0.1–0.3r_{500} is in good consistency with the value of 1.24 ± 0.04 keV, used in the *M*-*T* relation of Finoguenov et al. (2001).

Detailed measurements of the temperature and element abundance distribution in the studied systems allowed us to provide unbiased mean values for a range of group properties, which we list in Table 3. Column (1) lists the system name, column (2) the Galactic $N_{\rm H}$, which is fixed in the spectral modeling, column (3) the assumed luminosity distance, column (4) the implied scaling, column (5) the temperature, and column (6) metallicity as a fraction of the solar photospheric value, derived from a single region fit, with corresponding luminosity in the 0.5–2.4 keV band listed in column (7). Tables 4–5 list name of the system in column (1), mass average temperature in column (2), metallicity in column (3), volume averaged entropy in column (4), and pressure in column (5) using intervals $<0.1r_{500}$ and 0.1–0.3r_{500}, respectively.

We use the information derived from the maps as well as annuli to examine the radial variation of the properties of the hot gas. In Figure 3 we show the entropy and pressure profiles. These profiles have been scaled using r_{500} as calculated in Table 1, so that the profiles are on a common scale. The predicted entropy for the groups is shown as a dashed line and is derived from the scaling relationship of Ponman et al. (2003). To scale the data we use $(T_w/10\ {\rm keV})^{-2/3}$, where T_w is the mass-weighted temperature measured within 0.1–0.3r_{500}. We also examine the differences between the pressure profiles of the groups in our sample. As entropy, $Tn^{-2/3}$, scales as $T_w^{2/3}$, and density scales as $T_w^{1/2}$,

TABLE 4
PROPERTIES OF GROUPS WITHIN $0.1r_{500}$

Name	kT (keV)	Z ($Z_\odot$)	S (keV cm^2)	P (10^{-12} dyne cm^{-2})
NGC 2300	0.90 ± 0.01	0.22 ± 0.02	84 ± 4	1.77 ± 0.10
NGC 3665	0.54 ± 0.16	0.26 ± 0.31	44 ± 21	1.45 ± 0.70
IC 1459	0.61 ± 0.02	0.06 ± 0.01	25 ± 2	3.87 ± 0.34
NGC 3923	0.58 ± 0.13	0.27 ± 0.26	85 ± 34	0.65 ± 0.25
NGC 4168	0.72 ± 0.06	0.08 ± 0.04	92 ± 19	0.78 ± 0.18
NGC 4261	1.32 ± 0.02	0.21 ± 0.02	115 ± 4	2.75 ± 0.11
NGC 4636	0.79 ± 0.00	0.26 ± 0.01	58 ± 1	2.19 ± 0.04
NGC 5044	1.01 ± 0.01	0.73 ± 0.03	36 ± 1	10.3 ± 0.3
NGC 5322	0.64 ± 0.09	0.06 ± 0.06	56 ± 22	1.71 ± 0.65
NGC 5846	0.86 ± 0.01	0.38 ± 0.02	61 ± 2	2.77 ± 0.09

and thus the pressure scales as $Tn \sim T_w^{3/2}$. We then apply this scaling to the data, using $(T_w/10\ \mathrm{keV})^{-3/2}$, and display a typical pressure profile of the cluster scaled the same way in Figure 3.

The increase in entropy with increasing radius is roughly proportional to $r^{1.1}$. The adopted scaling is insensitive to the choice of the T_w, since it only adjusts the points parallel to the scaling. This is the advantage of entropy scaling. In Finoguenov et al. (2005) it is shown that clusters with cool cores follow the $r^{1.1}$ law and including all clusters flattens the trend. In addition to the clusters, we have included the entropy and pressure profiles obtained using the high-redshift subsample of Mulchaey groups (Finoguenov et al. 2006) to extend the result down to group scales. In Figure 3 the only group entropy profile that follows the $r^{1.1}$ law in the range $0.1 < r_{500} < 0.3$ is the NGC 5044 group. In the right entropy panel the NGC 5846 group lies above the scaling relation, and the NGC 4636 group data do not extend to a sufficiently large radius to determine whether it follows the scaling relation. In the right entropy panel only the NGC 2300 group might follow the entropy scaling at $r_{500} > 0.1$, but the outermost point is not consistent with $r^{1.1}$ scaling. Looking at the solid lines in Figure 3 for the group entropy profiles from Finoguenov et al. (2005), our low-redshift sample follows that scaling much more closely. However, the data for NGC 5044 and NGC 4636 lie systematically below the line for the average entropy profile, while in the right panel the groups have a higher average entropy than the Finoguenov et al. (2005) sample. One can further subdivide the groups based on those that have higher entropy at the center (e.g., NGC 4261) and those that have higher entropy at the outskirts (e.g., NGC 5322), compared to the plotted scaling relations. In both cases systematic deviations are also present in the pressure profiles.

The NGC 4636 group shows a higher pressure, compared to the mean, as also found in other cool core systems (Finoguenov et al. 2005). NGC 5044, NGC 5846, and NGC 4168 show pressure profiles consistent with the mean. The profiles of NGC 4261, NGC 2300, and IC 1459 initially decline more rapidly, but then become flatter and start to match the scaling for pressure. The remaining three groups show pressure profiles that decline more quickly than the typical profile. The significance of this can be seen by considering the response of the pressure to the large-scale state of the gas and gravitational potential, where $M/r \propto Tdlg(P)/dlg(r)$ and $P \propto M$, since both P and M scale with $T^{3/2}$. Lower pressure either indicates that the gravitational mass is low or that the temperature is enhanced at even larger radii. In the former case the total mass at r_{500} should be $1\text{–}5 \times 10^{12}\ M_\odot$. In the latter case some additional entropy input is required in excess of that predicted by the modified entropy scaling. This additional entropy is needed on scales exceeding $0.3r_{500}$ (approximately 150 kpc in these groups; see Fig. 3).

Another way to look at the results described above is to present the normalization and the slope of the entropy and pressure profiles (Table 6). To deal with the nonstatistical scatter of the points, we applied the bisector method and orthogonal regression, following Helsdon & Ponman (2000), and we present the results obtained using the latter method in Table 6, while monitoring the difference between the methods. Once the general behavior of the entropy and pressure was found, we studied the amplitude of the deviations from the fit and compared that with the statistical errors in Table 7 for the systems with the best statistics. In addition to fitting the power laws to the pressure and entropy profiles, we provide in Table 7 the scatter around the mean trend for the groups from Finoguenov et al. (2006), in which we allowed a renormalization of the model. In general, the structure in both entropy and pressure maps amounts to 10%–20%. Stronger deviations, seen in NGC 2300, are located in the area between the two major galaxies, indicating an interaction between the two

TABLE 5
PROPERTIES OF GROUPS BETWEEN $0.1r_{500}$ AND $0.3r_{500}$

Name	kT (keV)	Z ($Z_\odot$)	S (keV cm^2)	P (10^{-12} dyne cm^{-2})
NGC 2300	0.75 ± 0.01	0.48 ± 0.19	161 ± 19	0.39 ± 0.07
IC 1459	0.59 ± 0.03	0.09 ± 0.03	108 ± 19	0.41 ± 0.08
NGC 4168	0.77 ± 0.31	0.00 ± 0.05	155 ± 73	0.44 ± 0.24
NGC 4261	1.11 ± 0.02	0.17 ± 0.01	164 ± 6	0.98 ± 0.04
NGC 4636	0.77 ± 0.01	0.15 ± 0.01	86 ± 3	1.10 ± 0.05
NGC 5044	1.21 ± 0.01	0.38 ± 0.02	86 ± 2	3.31 ± 0.09
NGC 5846	0.69 ± 0.01	0.19 ± 0.03	116 ± 13	0.54 ± 0.05

TABLE 6
Characteristics of Entropy and Pressure Profiles for the Sample

Name	$S(0.2r_{500})$ (keV cm^2)	S Slope	$P(0.2r_{500})$ (10^{-14} dyne cm^{-2})	P Slope
NGC 2300	163 ± 10	0.80 ± 0.10	46 ± 2	−1.17 ± 0.08
NGC 3665	116 ± 80	0.64 ± 0.48	8 ± 4	−1.58 ± 0.44
IC 1459	136 ± 6	0.81 ± 0.05	46 ± 5	−1.08 ± 0.20
NGC 3923	210 ± 20	1.07 ± 0.17	17 ± 5	−1.44 ± 0.26
NGC 4168	90 ± 10	0.20 ± 0.13	50 ± 8	−0.72 ± 0.18
NGC 4261	288 ± 32	0.87 ± 0.15	95 ± 6	−0.98 ± 0.14
NGC 4636	131 ± 5	0.81 ± 0.03	66 ± 1	−1.07 ± 0.04
NGC 5044	104 ± 2	0.82 ± 0.04	284 ± 13	−0.78 ± 0.07
NGC 5322	337 ± 23	0.77 ± 0.26	6.5 ± 2	−1.29 ± 0.34
NGC 5846	116 ± 6	0.87 ± 0.05	58 ± 2	−1.26 ± 0.05

dominate galaxies in this group. The relatively high level of fluctuations in NGC 4261, discussed in more detail below, seem to be associated with the AGN activity.

4.2. *Origin of the X-Ray Emission*

The *XMM-Newton* data allow us to compare the entropy and pressure behavior at radii exceeding $0.1r_{500}$ for a large sample of groups for the first time. Based on the levels of entropy and pressure plotted in Figure 3, which are further confirmed in normalization of the pressure in Table 6, we conjecture a subdivision of our sample into two broad categories. We base our division on X-ray properties at $0.2r_{500}$. This results in groups whose properties are largely defined by gas accretion ("ADAGE" groups, for accretion dominated average group environment) and systems whose diffuse thermal X-ray emission is not wholly associated with the accretion of the gas on potential wells of the group. The first category is also speculated to be baryonically closed groups based on the extrapolations of Mathews et al. (2005). Inside $0.2r_{500}$, we report large deviations in the mean values for entropy and pressure between the ADAGE groups (Table 6), which suggests further refinement of the definition. We call NGC 5044 and NGC 5846 regular groups (or cooling core groups) because of low scatter in their pressure and entropy profiles. In addition, these systems follow the expected entropy scaling relation, shown in Figure 3. Although the central properties of NGC 4636 also follow the scaling relations, large deviations are seen at $0.2r_{500}$ radius, which we attribute to an interaction with the Virgo Cluster. Many underluminous ADAGE groups are similar to regular groups at large radii. These are IC 1459, NGC 2300, NGC 4168, and NGC 4261. For NGC 2300 and NGC 4261, for which the two-dimensional analysis was possible, we measure a large degree of disturbance in their gas properties. NGC 2300 might be experiencing a merger, while NGC 4261 has signatures of ongoing AGN activity.

To the second category of objects belongs NGC 5322, and perhaps NGC 3923, based on our failure to detect emission at $0.2r_{500}$. Although there is a large uncertainty in parameters derived for the NGC 3665 group, it exhibits extremely low galaxy velocity dispersion for its temperature, and we include it into this category.

As the division is entirely based on the entropy level, a system of low X-ray luminosity is considered a group if its temperature is proportionally low, while a different origin of the emission is suggested if the temperature is high. With the current data in hand, these two categories do not overlap in the entropy at radii exceeding $0.3r_{500}$.

ADAGE groups are virialized objects, whose thermodynamic properties of the X-ray-emitting gas have been determined by the accretion of gas into the potential well of the group. Arguments on the conversion of neutral H I gas to hot X-ray-emitting gas (Trinchieri et al. 2003) indicate that the nature of X-ray emission in the compact group HCG 92 is different. The importance of defining ADAGE is that a similar approach is adopted for simulations (e.g., Borgani et al. 2005). The weakest point, shared by all X-ray studies of groups, is that the low-mass clusters and groups show substantial deviations from the scaling laws predicted by pure gravity. Thus, a common approach in the modeling is to tune various feedback effects so that the simulations reproduce the observed X-ray properties of the groups. A subdivision, attempted in this paper, is aimed at outlining the potentially different origin of the X-ray emission of a subclass of X-ray-underluminous groups, which is usually considered in simulations looking into the formation of early-type galaxies (e.g., Burkert & Naab 2004), while on the other hand producing a sample of

TABLE 7
Entropy and Pressure Fluctuations around the Best Fit

	Power Law (%)		Averaged Group Profile (%)		
Name	σS	σP	σS	σP	Comment
NGC 2300	25 ± 6	126 ± 15	24 ± 6	171 ± 22	
NGC 3923	31 ± 8	25 ± 12	18 ± 12	36 ± 8	
NGC 4261	21 ± 2	17 ± 2	15 ± 1	20 ± 2	
NGC 4636	24 ± 1	22 ± 2	20 ± 1	21 ± 2	Including the plume
NGC 4636	11 ± 1	23 ± 3	16 ± 1	31 ± 2	Central 5′
NGC 5044	10 ± 2	13 ± 2	12 ± 3	8 ± 2	Central 5′
NGC 5846	13 ± 2	16 ± 3	14 ± 1	12 ± 3	

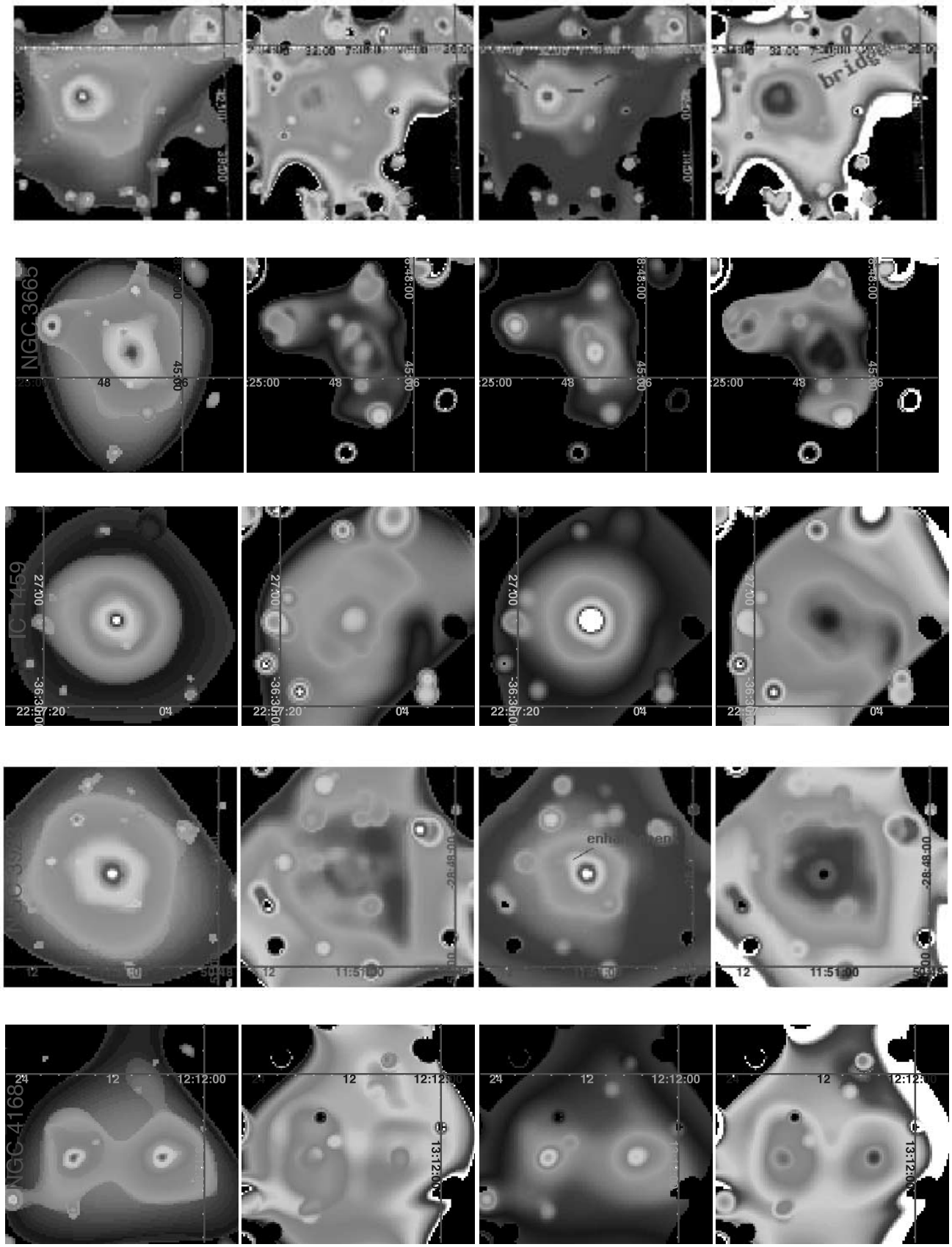

Fig. 4.—*Left to right:* Surface brightness, temperature, pressure, and entropy maps of the groups. *Top to bottom:* NGC 2300, NGC 3665, IC 1459, NGC 5322, NGC 4168; NGC 4261, NGC 4636, NGC 5322, NGC 5044, and NGC 5846.The temperature, pressure, and entropy maps in this figure are based on the hardness ratio analysis. The values for the pseudo entropy and pressure maps are arbitrary, while their absolute values as well as the significance of all the features are obtained through the subsequent spectral analysis, which we both tabulate and report in the text. The features not discussed in the text are regarded as marginal. All the figures have the same color scale for the same quantity. Temperature coding ranges from black to white, corresponding to 0.3–1.6 keV. On the panel corresponding to the pressure image of NGC 2300, the straight lines demarcate the bow-shaped enhancement, and the bridge in the entropy map of NGC 2300 is labeled. Enhancement in the pressure map of NGC 3923 is marked. The bow on the images of NGC4636 is marked. On the panel corresponding to the pressure image of NGC 5846, the straight line demarcates the ring-shaped enhancement. The levels of the surface brightness could be read from Fig. 5. [*See the electronic edition of the Journal for a color version of this figure.*]

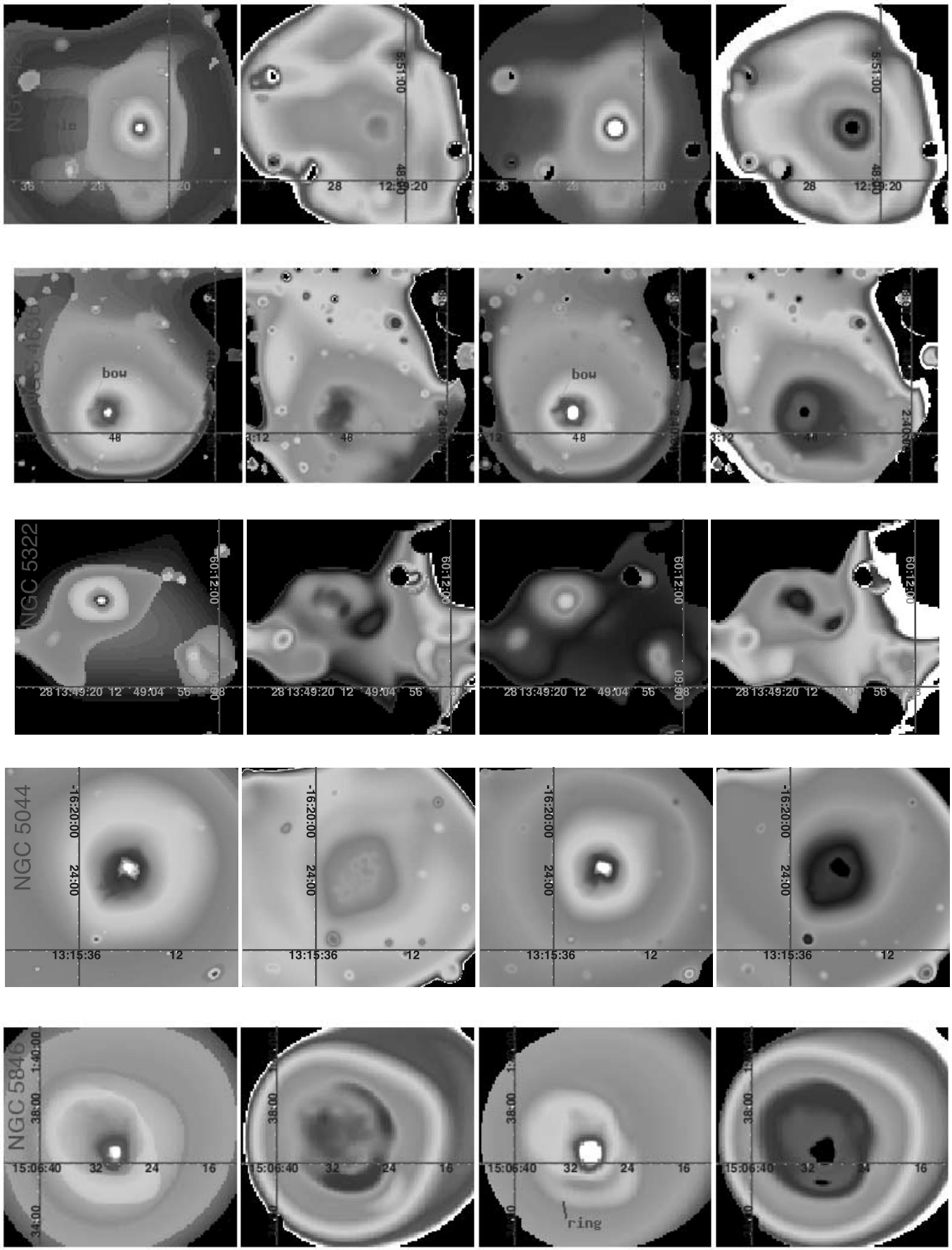

FIG. 4.—*Continued*

objects whose properties could be compared to cluster-type simulations of, e.g., Borgani et al. (2004).

The entropy levels of the second category of objects are up to a factor of 3 higher than the other groups in our sample, as illustrated with NGC 5322 in Figure 3 and the *ASCA* sample of Ponman et al. (2003). The low pressure (up to a factor of 10) and high entropy at all radii in these systems cannot be explained by infall of gas associated with group formation. Thus, it is probably more likely that the X-ray emission in these systems originates from the interstellar medium of the galaxies and not as infalling gas. We can infer by looking at the normalization of the pressure profiles that most of the systems in question have masses about 10% of the NGC 5044 group, which places them in the $10^{12}\ M_{\odot}$ range. This is more typical of massive elliptical galaxies. The existence of such objects suggests that the mere presence of a faint X-ray emission in a system can be misleading. In particular, the presence of X-ray emission in a group does not always mean that the system is a virialized object, and the nature of these groups is still unclear. To complete the global properties of this category of groups, we note that the element abundance observed in the X-ray gas is very low, and this (assuming the robustness of optical metallicity indicators) contradicts the suggestion that all the gas originates from stellar mass loss. Additional insights into the origin of this component have been provided by the higher redshift part of this survey, which includes HCG 92 (Finoguenov et al. 2006), for which Trinchieri et al. (2003) argue that shock heating of an H I cloud is now generating the X-ray-emitting group gas. They reach the conclusion that the faint diffuse X-ray component is from a galaxy interacting with the group. We note that NGC 5322 has a counterrotating core, which is most certainly a result of a recent merger. The high entropy level of the observed component requires cooling times longer than the Hubble time to remove the high-entropy gas (e.g., Voit et al. 2003). So we expect the faint X-ray halo to be an indicator for and a fossil record of the merger history of early-type galaxies. These arguments can also be extended to the faint X-ray halos of postmerger galaxies reported in Read & Ponman (1998). On the other hand, spiral dominated groups studied here (NGC 7582) and in the literature (Mulchaey et al. 1996) do not have detected extended X-ray emission on 100 kpc scales, with first detections of extended emission on 20 kpc scales by Pedersen et al. (2006). This may indicate that the majority of spiral-rich groups neither possesses large mass halos nor has undergone the galaxy-galaxy interactions needed to form a diffuse hot halo, similar to X-ray-faint groups such as NGC 5322 and HCG 92.

4.3. *Maps*

In this section we present the surface brightness, temperature, projected pressure, and entropy maps (see Fig. 4, where the details of the map construction are described). Overlays with DSS2 *R*-band images are shown in Figure 5, and individual systems are discussed in the following subsections. Although the maps present projected properties, they could be shown to give an insight on the three-dimensional properties (Schuecker et al. 2004; Dolag et al. 2005).

5. DISCUSSION

Before discussing the individual systems, we outline the sources of variations seen in the maps in Figure 4. Among the four maps presented, only two are independent and in principle sufficient for the analysis. Although surface brightness analysis and temperature maps are more commonly used in studies of groups and clusters, pressure and entropy maps are more straightforward to interpret. The pressure traces the generalized stress tensor, which in the case of a system in hydrostatic equilibrium and without dynamically important magnetic fields is given by the gravitational potential. Departures from equilibrium are likely to be local, i.e., seen as pressure fluctuations on the map. Common examples include shocks (e.g., Markevitch et al. 2002; Jones et al. 2002; Henry et al. 2004; Finoguenov et al. 2004a, 2004b) and pressure waves (e.g., Fabian et al. 2003; Schuecker et al. 2004). Substructure can also be seen in pressure maps as secondary peaks, provided that it retains its own gas or it moves subsonically. The entropy map for a system in equilibrium should be symmetrical around the center and exhibit an increasing entropy level with increasing radius. Deviations in the entropy maps in the form of low entropy gas displaced from the center are either due to development of instabilities (e.g., cold fronts in A3667 [Vikhlinin et al. 2001] and in A3562 [Finoguenov et al. 2004a]; shear instability in A3667 [Mazzotta et al. 2002; Briel et al. 2004]), which are slow to relax (0.2 of the sound speed; Ricker & Sarazin 2001) or the result of stripping (M86; Finoguenov et al. 2004b). These are examples of low-entropy gas displaced from the center. Off-center low-entropy zones associated with local gravitational minima (e.g., secondary pressure peaks, or simply galaxies, as in Finoguenov et al. 2004c), are indicators of substructure. In addition, areas of high-entropy gas, found surrounding low-entropy gas (so called buoyant bubbles) are produced by in situ heating, most likely by AGNs (see, for example, NGC 4261 below).

Since the X-ray emission of groups is strongly dominated by Fe lines, the maps are also affected by patchy metallicity distributions. In our discussion below of individual features, we deconvolve the effects of enhanced density from the effects of the enhanced metallicity or indicate where this separation is not obvious. Patchiness of the metallicity distribution has not been studied in detail before and could be an important factor indicating the processes of the metal release into the intragroup medium. One of the well-established examples of such a process is the gas entrainment by the jet-induced instabilities in M87 (Churazov et al. 2001), which brings low-entropy, high-metallicity gas from the inner kiloparsecs of M87 out to 50 kpc radius.

The systematic analysis of the metallicity distribution using the regions in NGC 4636, NGC 5044, and NGC 5846 is reported in Table 8. With the typical size of the resolution element of 2–10 kpc, sampling the area within 20–50 kpc from the brightest group galaxy, we find that the profiles are consistent with a linear decrease with radius, reaching 0.3 solar value by $0.05r_{500}$. The scatter of points around the best fit is high, 30%–50%, which characterizes the degree of patchiness on 20–50 kpc scales.

5.1. *NGC 2300,* $z = 0.0046$

The pressure and entropy structure consists of two blobs, centered on NGC 2300 and NGC 2276. The pressure map contain a large-scale bow-shaped enhancement outside the low-entropy gas centered on NGC 2300. Such gas compressions are possible in several cases: supersonic motion of NGC 2300 with respect to the group; supersonic interaction between NGC 2300 and NGC 2276; or the presence of substructure around NGC 2300. In any case, the dispersion in the pressure map of NGC 2300, reported in Table 7, is high in comparison to other groups. Since this does not seem to be an effect of confusion with a background object, as is sometimes the case (Mahdavi et al. 2005), we suggest, based on a similar work applied to simulations (A. Finoguenov et al. 2006, in preparation), that the NGC 2300 group exhibits the signs of a merger. The pressure and entropy deviations 2′ southwest of the center may be explained if there is ongoing gas

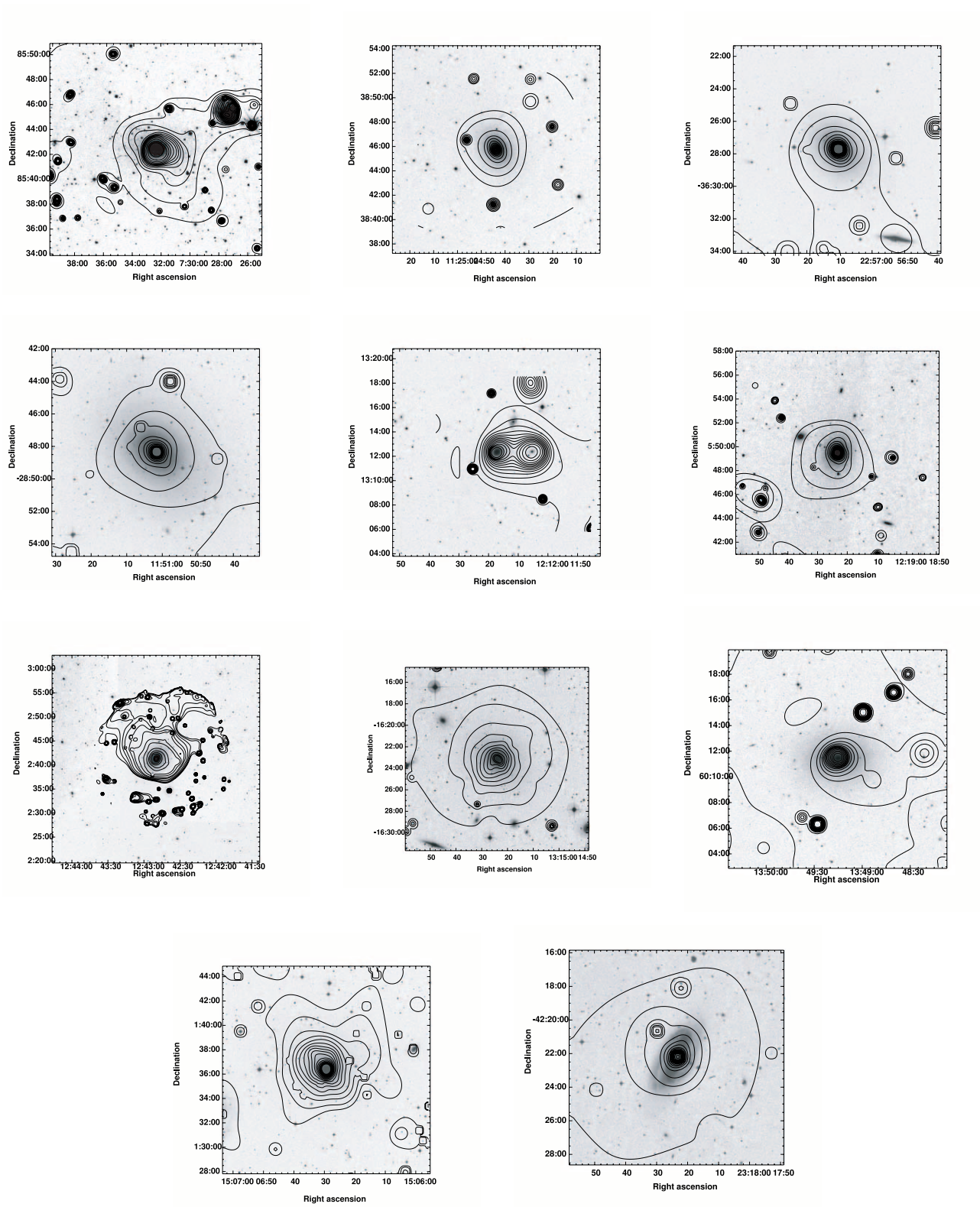

FIG. 5.—DSS2 *R*-band images of the groups overlaid with contours indicating levels of X-ray emission, as obtained by the adaptive smoothing. *Top left to lower right:* NGC 2300, NGC 3665, IC 1459, NGC 3923, NGC 4168, NGC 4261, NGC 4636, NGC 5044, NGC 5322, NGC 5846, NGC 7582. The X-ray contours are in units of MOS1 count pixel^{-1} (pixels are 4″ on a side) and drawn on the following levels: 0.2–0.4–0.5–0.6–0.7–0.8–0.9–1.1–1.3–1.4–1.7–2.1–3.2–4.8 (NGC 2300); 0.10–0.12–0.2–0.3–0.5–0.8–1.0–1.4–1.8–2.3–2.8–3.4–4.0–4.6–5.4 (NGC 3665); 0.1–0.2–0.4–0.7–1.1–1.6–2.3–3–4–5–6–7–9–10–12–13–15 (IC 1459); 0.2–0.3–0.8–2–3–4–6–8–10 (NGC 3923); 0.08–0.10–0.13–0.15–0.17–0.19–0.22–0.24–0.26–0.29–0.32–0.35–0.39–0.6 (NGC 4168); 0.22–0.27–0.3–0.4–0.6–1.1–1.4–2–3–4–5–7–9–11 (NGC 4261); 0.87–0.95–1.0–1.2–1.4–1.7–2–3–6–9–19–39–57–116 (NGC 4636); 0.3–0.6–1.4–3–5–7–10–14–18–23–28 (NGC 5044); 0.04–0.06–0.07–0.08–0.10–0.12–0.14–0.20–0.35–0.5–0.9 (NGC 5322); 0.2–0.3–0.7–1.3–2–3–5–6–8–10–13–15–18–21–24–28 (NGC 5846); 0.16–0.17–0.19–0.21–0.25–0.30–0.35–0.42–0.5–0.6–0.7–0.8 (NGC 7582). In each figure the lowest contour level is selected to be $\sim$4 σ above the background.

TABLE 8
Fe Abundance Trends and Scatter

Name	Fe ($0.05r_{500}$)	Fe Slope	σ Fe (%)	Comment
NGC 4636	0.46 ± 0.06	-0.4 ± 0.2	45 ± 6	Central 5′
NGC 5044	0.68 ± 0.06	-0.3 ± 0.1	25 ± 6	Central 5′
NGC 5846	0.34 ± 0.09	-0.9 ± 0.3	41 ± 6	

accretion from the south. NGC 2276 (Arp 25) is considered a strongly interacting object (Gruendl et al. 1993; Hummel & Beck 1995), which supports our suggestion on the supersonic interaction. The line-of-sight velocity difference between NGC 2276 and NGC 2300 amounts to 503 ± 7 km s^{-1}, which is supersonic with respect to the sound speed for the intergalactic medium (IGM) temperature of 0.7 keV. In general, late-type spiral galaxies are considered to be currently infalling and moving on radial orbits (Biviano & Katgert 2004).

There is an entropy bridge toward the second galaxy (NGC 2276), suggesting absence of a large line-of-sight separation between the two. This implies that gas in the halo of the spiral galaxy is interacting with IGM of the group.

Spectroscopic results suggest that apart from the very center of the elliptical and 1′ around the spiral, the temperature distribution is nearly isothermal. Extensions of the pressure to the southwest and to the west are confirmed and are evaluated to be a factor of 1.33 ± 0.05 enhancement. The extension of the low-entropy zone to the southwest is characterized by a $10\% \pm 1\%$ lower entropy and the entropy bridge, which has an entropy of 50 ± 10 keV cm^2, is a factor of 2 lower, both compared to a typical entropy at the same distance to NGC 2300, estimated from the annuli.

5.2. *NGC 3665*, $z = 0.0069$

The bright part of the emission extends to 3′ in radius, centered on NGC 3665, and has a similar elongation as the galaxy's major axis. There is also a very bright background AGN east of the galaxy. Due to lack of counts, the spectral analysis was done on four zones that are symmetric around the center, which precludes revealing any two-dimensional structure.

5.3. *IC 1459*, $z = 0.0057$

IC 1459 is a well-studied elliptical galaxy with a known hard X-ray component suggestive of an AGN (Matsumoto et al. 1997). Recent *Chandra* observations of this system reveal that the nuclear X-ray source has a luminosity $L_X = 8 \times 10^{40}$ ergs s^{-1} in the 0.3–8 keV band and a slope $\Gamma = 1.88 \pm 0.09$ (Fabbiano et al. 2003).

In carrying out the spectral analysis we have accounted for the presence of the AGN in IC 1459 by introducing a variable slope power-law component with a variable absorption in our spectral fits for the central region. The presence of the bright point source at the center of the group complicates the spectral analysis. We find a significant temperature variation 3′ distance from the center, rising from 0.3 ± 0.1 to 1.0 ± 0.2 keV, with the hotter temperature observed to the northwest and southeast of the galaxy. Additional attempts to further quantify the substructure in this compact system were stymied by the point source in the center, the relatively large wings in the PSF, and the low number of counts in the diffuse gas. Outside the region of the temperature rise, the group gas has a constant temperature profile, at least within the temperature error, while the other fitted quantities can vary significantly. But with the contribution of the scattered photons from the central point source we reserve judgment on the physical nature of the variations. In addition to the *XMM-Newton* data there is also a *Chandra* observation of this system. It may provide insight into the diffuse gas, but that analysis is beyond the scope of this paper.

5.4. *NGC 3923*, $z = 0.0069$

The central galaxy of this group, NGC 3923, is a nearby early-type galaxy classified as E4 (RC3). This galaxy has numerous shell structures (Malin & Carter 1983), indicating past merger activity, but shows no signs of an AGN.

The X-ray surface brightness of this group has a regular appearance, and the X-ray emission can be traced to about 5′. This group shows the presence of numerous point sources, which somewhat complicates the analysis. NGC 3923 has previous *ROSAT* PSPC and High Resolution Imager (HRI) data. The PSPC spectral results are for two zones out to 2′ and show no evidence for a temperature gradient (Buote & Canizares 1998) at the level of 0.50 ± 0.05 keV. The *ASCA* data for a slightly larger region indicate a slightly higher best-fit temperature of 0.64 ± 0.07 keV (Sato & Tawara 1999), yet a two-component fit yields a temperature of 0.55 keV (Buote & Fabian 1998). The *XMM-Newton* data reveal a temperature structure within 2′ consisting of patches of lower (0.35 ± 0.05 keV) temperature and an approximately constant temperature outside this region at the level of 0.56 ± 0.01 keV. We note that we include a hard component as part of the fit to account for the contribution of unresolved LMXBs.

The results of the spectroscopic analysis reveal that variations in the temperature are associated with the presence of the gas with entropy lower than the value expected by interpolating other points. Such low-entropy regions could, for example, be produced by gas entrainment during preceding jet activity and have not yet settled down. An alternative explanation may be that merger activity can inject low-entropy gas. The statistical analysis, reported in Table 7, concludes that the statistically significant fluctuations are only seen in the entropy.

Overall, the pressure map shows a fairly symmetric structure. There is a small enhancement 0.′5 to the northeast of the galaxy, which is blended with the central emission and cannot be separated spectrally for an independent analysis. This enhancement is visible on the temperature map and may show up faintly in the entropy map. Overall the entropy map appears quite symmetric as well. The overlay of the X-ray surface brightness contours on the optical image shows the enhancement in the pressure corresponds to the direction of the major axis of the galaxy and therefore might be associated with triaxiality of the gravitational profile.

5.5. *NGC 4168*, $z = 0.0077$

The two peaks in the pressure and entropy maps correspond to the two bright galaxies in the *XMM-Newton* FOV. The pressure map does not show any sign of hydrodynamic interaction between those two galaxies and is elongated to the north, possibly indicating the direction of the gas accretion.

Lack of counts precludes a detailed analysis of this group. The galaxy to the west (NGC 4164) turns out to be a background galaxy ($V_H = 17{,}500$, while the central galaxy in this group, NGC 4168, has a velocity of $V_H = 2784$). While a discrimination of the background galaxy is trivially done by separating them in

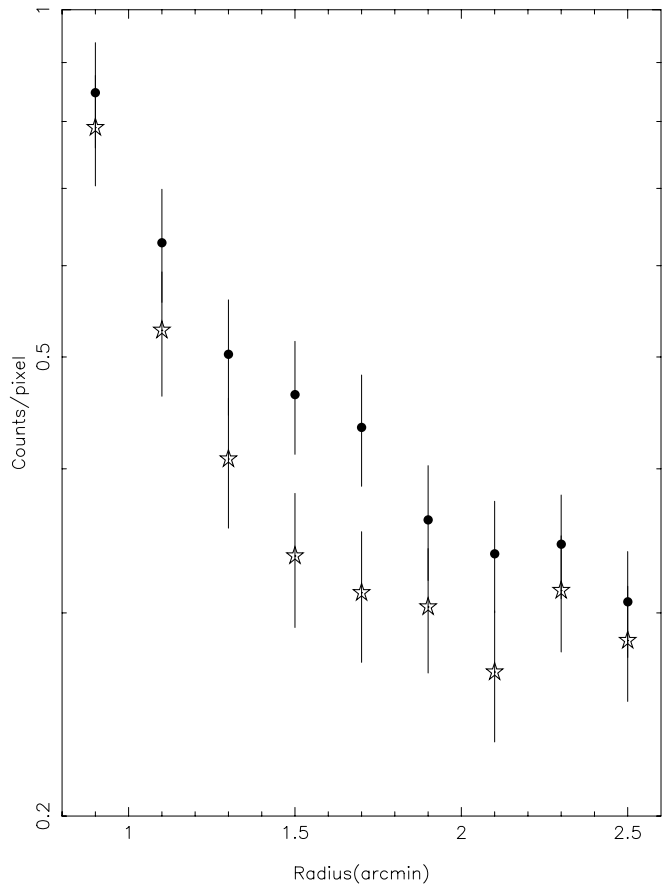

FIG. 6.—Surface brightness profile in NGC 4261. The circles (*stars*) demarcate the profile in the north-south (east-west) direction. The figure zooms in to the spatial region, where differences are seen, while the profiles are identical within the central 20″ and outside 3′.

the velocity space, the important point is that we were able to separate the effects of projection from the interaction.

5.6. *NGC 4261, z* = 0.0068

X-ray emission of NGC 4261, also reported in Gliozzi et al. 2003, extends over the whole *XMM* FOV. Both pressure and entropy maps appear symmetric with some elongation in the north-south direction. The spectroscopic analysis confirms the extension in the pressure in the north and south directions. Overall, the very high temperature (1.0–1.5 keV) and low luminosity of the system yield very high entropy levels.

The differences between the north-south and the east-west directions are clearly seen in the surface brightness reported in Figure 4, as well as in the profile shown in Figure 6. The profiles are identical within the central 20″ and outside 3′. An explanation to the peculiar emission in NGC 4261 is offered through the comparison with the radio data, as is seen in Figure 7, the radio lobes fill the space between the X-ray emission. The presence of the radio bubble introduces an additional pressure at the level of 2×10^{-12} dyne cm^{-2}. Detailed analysis shows that the thermal gas inside the eastern bubble is in pressure equilibrium with its immediate surroundings. The gas inside the bubbles is characterized by a higher entropy 98 ± 9 keV cm^2 to the east and 105 ± 11 keV cm^2 to the west, compared with 85 ± 6 keV cm^2 at similar distance to the center as well as 30 ± 3 keV cm^2 in the central 10 kpc. The western bubble has lower pressure compared to surroundings, indicating the importance of the relativistic particle energy. Our measurements support the claim of Croston et al. (2005) in regard to finding the direct evidence of AGN reheating of gas in groups. We note a remarkable similarity in the optical properties of NGC 4261 and NGC 5322; they have similar absolute *B* magnitudes (derived using the distance measurements from Tonry et al. 2001 and the corrected *B* magnitude from RC3), −19.52 and −19.84, respectively, they

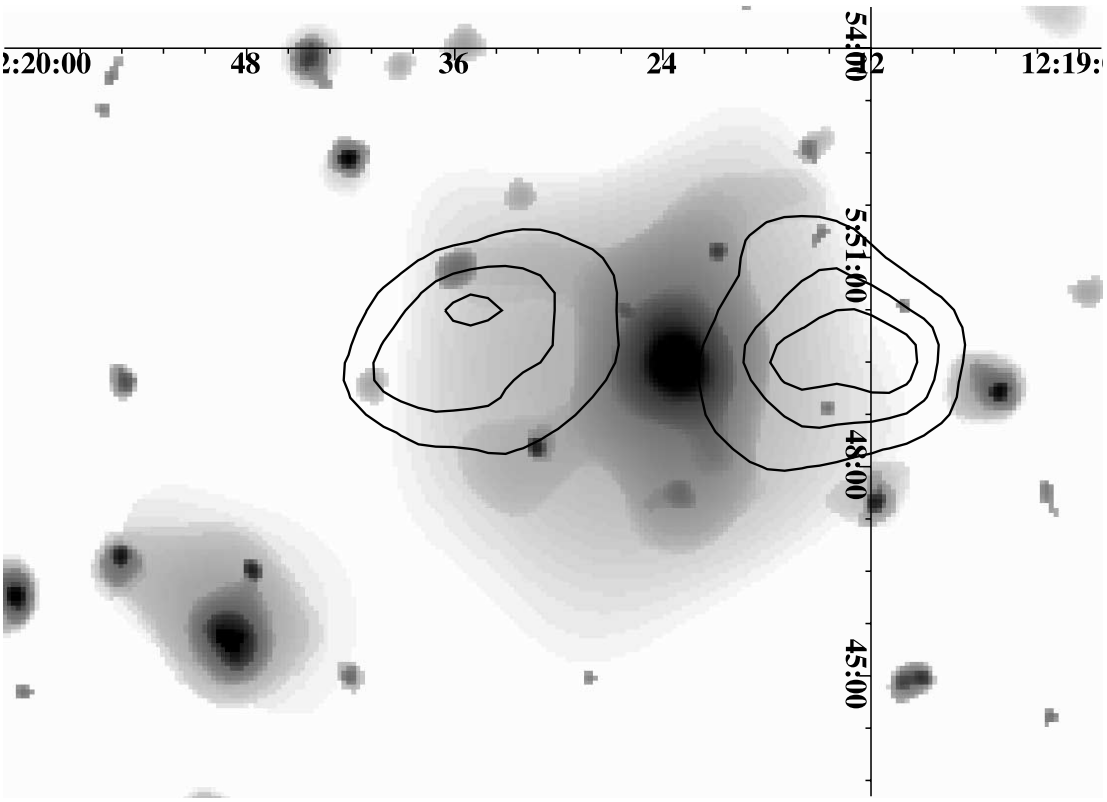

FIG. 7.—Wavelet-reconstructed X-ray image of NGC 4261, overlaid with the radio contours.

FIG. 8.—Iron abundance maps of NGC 4636, NGC 5846, and NGC 5044 (*left to right*). Violet represents the Fe abundance level of 0.1 solar, and values for the other colors are blue: 0.2 solar; green: 0.3 solar; red: 0.5 solar; and white: above 0.8 solar. A typical uncertainty is less than 0.1, which is smaller than the color separation.

are both classified as liners, and the effective radii are similar, $\log r_e = 1.59$ and 1.54, respectively. In addition the colors are similar $\Delta(B - R) = 0.03$, as are the color gradients (Michard 1999). Yet, the entropy of the gas at the center of NGC 4261 is a factor of 4 larger (the entropy in the core of NGC 5322 is 6.5 ± 2 keV cm^2). As the gas properties at the center are dominated by stellar mass loss, which is expected to be the same between the two galaxies, the observed difference measures the degree of impact the AGN has on the interstellar medium.

5.7. *NGC 4636, z* = 0.0044

NGC 4636 has been classified as a very symmetric, E0, elliptical galaxy (RC3) based on the optical analysis of the central region. However, at larger radii the optical isophotes become increasingly elliptical (King 1978). The *Einstein* IPC image of this galaxy reflects the optical morphology with very symmetric emission near the center and asymmetry on larger scales (Forman et al. 1985; Stanger & Warwick 1986). The *ROSAT* PSPC data show a flattening of the X-ray surface brightness profile starting about 4′ to the northeast of the galaxy center (Trinchieri et al. 1994).

The *XMM-Newton* data show this flattening of the profile at the same position as the PSPC data. Examining the pressure map near this location we identify a peculiar inward-pointed bow-shaped enhancement also ∼4′ to the northeast from the center. We find no associated entropy dip with any of these pressure enhancements. This might indicate the presence of a shock. Similar conclusions have been reported using *Chandra* observations (Jones et al. 2002).

The entropy map shows complex structures that are well correlated with structures seen in the pressure map in the inner 3′. At larger radii the entropy map shows fewer distinct features. One possible explanation for the small-scale features might be that foreground or background objects are contributing to the X-ray emission at these locations. However, the DSS optical image does not reveal any optical object corresponding to the identified pressure and entropy features.

The most striking large-scale feature of NGC 4636 is the strong enhancement of the emission 10′ to the north from the center, which we refer to as a plume (Fig. 9). Although appearing on the edge of the *XMM-Newton* FOV, this emission is also seen in *ROSAT* data. The optical data do show that there is a small galaxy concentration to the north of the galaxy. Redshift information from the NASA/IPAC Extragalactic Database (NED) shows that this group has a redshift of $z = 0.07$, but this system does not coincide with features in the maps. Moreover, an association with the polar spur appears unlikely, as no peculiarity is seen in the infrared maps. Furthermore, the parameters of the emission (0.6 keV) are not typical of that of the spur (0.3 keV). In addition, we have examined the RASS data, and this is not part of a larger scale feature that extends beyond the *XMM-Newton* FOV.

The results of spectral analysis reported in Figures 8–9 show that the plume has a similar pressure to the surroundings, and it has a low element abundance consistent with its surroundings. However, the entropy is low when compared to the surrounding gas and indeed shows some of the lowest entropy in the NGC 4636 system. One explanation is that this is low-entropy group gas. Analysis of the pressure map indicates an azimuthal variation in the pressure at 3′ radius from the center, possibly related to the origins of the plume. Low-entropy gas is seen to the south and west of the galaxy center. The structure of this low-entropy gas is reflected in the iron abundance maps and can be seen as a region of high abundance. The plume to the north of the galaxy is a sign that NGC 4636 is undergoing stripping. Recent *Chandra* observations have revealed a cold front on the southern part of NGC 4636 (C. Jones 2004, private communication), which, on one hand, is an additional argument supporting our association of the plume with the ongoing stripping process and, on the other, favors a core oscillation scenario (e.g., Tittley & Henriksen 2005) as the origin of interaction. In the case of NGC 4636, the core oscillation could be caused by the gravitational pull of the Virgo supercluster, a suggestion that could be tested using numerical simulations. The iron abundance map, presented in Figure 8, reveals a strong contrast in the metallicity. The metallicity inside the central 1.′5 (5.9 kpc) varies between 0.5 and 1.0, with a typical error of 0.05 and a typical element resolution of 2 kpc. At 2.′6 distance from the center the metallicity reaches 1.1 ± 0.1 value (*shown in red*). The high-metallicity zone has a stronger extension toward the southwest. The metallicity of the plume is much lower, 0.13 ± 0.01, but is comparable to the zone outside the core at a similar (12′) distance to the center, studied with annuli.

Our reinvestigation of the group membership suggests the absence of galaxies at velocities similar to NGC 4636. On the other hand, the arguments of the X-ray analysis infer that NGC 4636 has a group-size halo, which confirms a conclusion of Matsushita et al. (1998) attributing NGC 4636 to fossil groups,

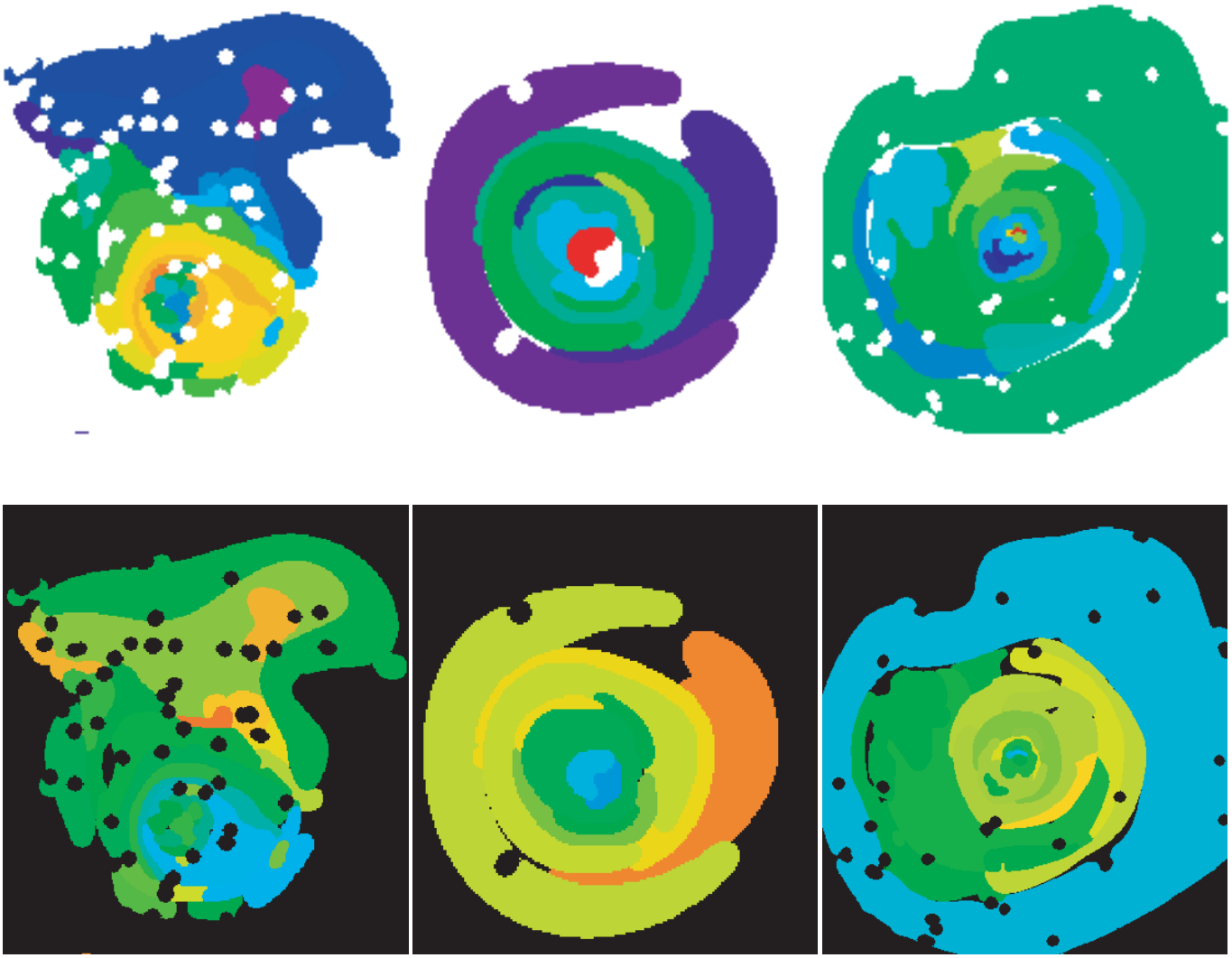

FIG. 9.—Maps of the ratio between entropy (*top*), pressure (*bottom*), and mean trend of the corresponding quantity with radius, measured for NGC 4636, NGC 5846, and NGC 5044 (*left to right*).

a recently emerged class of objects (Ponman & Bertram 1993; Vikhlinin et al. 1999; Mulchaey & Zabludoff 1999).

5.8. *NGC 5044*, $z = 0.0082$

The two-dimensional spectral mapping of the properties of the X-ray emission from NGC 5044 is done at the effective 4–10 kpc resolution, within the central 50 kpc. The temperature map of NGC 5044 (Fig. 4) reveals a cool zone 1′ southeast from the X-ray center. The parameters of this zone are as follows: $M_{\rm gas} = 2 \times 10^9\ M_\odot$, $kT = 0.82 \pm 0.01$ keV, Fe $= (0.9 \pm 0.1)$Fe$_\odot$, $S = 19 \pm 1$ keV cm^2, $P = (1.1 \pm 0.2) \times 10^{-11}$ dyne cm^{-2}. This feature has been seen in the analysis of the *ROSAT* data by David et al. (1994), who associate its appearance with a cooling wake. The idea was that the motion of NGC 5044 in the cooling gas of its group creates an enhancement of the dropping-in gas behind the galaxy. However, the assumption of the cooling flow used in that scenario is no longer a preferred interpretation of the data (e.g., Tamura et al. 2001). *XMM-Newton* data, shown in Figures 8–9 reveal that the wake has a lower entropy compared to both the mean trend for the atmosphere of NGC 5044 and to the entropy of the gas located on the opposite side from the center. On the other hand, the entropy of the wake is similar to the entropy of the gas at the center, which suggests a similar origin. The characteristics of the central region where a similar mass of the gas is encompassed are as follows: $kT = 0.81 \pm 0.01$ keV, Fe $= (0.82 \pm 0.05)$Fe$_\odot$, $S = 14 \pm 1$ keV cm^2, $P = (1.9 \pm 0.1) \times 10^{-11}$ dyne cm^{-2}. The parameters of the gas at the same distance to the center as the wake are $kT = 0.97 \pm 0.01$ keV, Fe $= (0.66 \pm 0.05)$Fe$_\odot$, $S = 29 \pm 1$ keV cm^2, $P = (0.97 \pm 0.05) \times 10^{-11}$ dyne cm^{-2}. High metallicity in the wake, detected by *XMM-Newton*, also supports a conclusion of the same origin of the gas in the wake and in the center of NGC 5044. After re-examining the origin of the wake, we conclude that both the motion of the galaxy (e.g., due to the core oscillations) and former AGN activity can provide an explanation. The extent and form of the entropy wake of NGC 5044, shown in Figure 9, supports the gas-stripping hypothesis. The reported deviations bear a local character, while the statistical analysis run within the 5′ radius from the center (Table 8) confirms the regularity in the pressure distribution. A dispersion in the Fe abundance (Table 7) is higher than the dispersion in the entropy (Table 7), indicating different origins of the gas that shares the same state. Indeed, stellar mass loss of the central galaxy, stripping of the group members, as well as the low-entropy part of the intragroup medium are very

close in their gas characteristics, yet each poses a different metallicity. We conclude that *XMM-Newton* supports the work on using the metallicity as a tracer of the formation of IGM (e.g., Schindler 2004).

5.9. *NGC 5322, z* = 0.0065

The central galaxy NGC 5322 is a bright, E3 galaxy (RC3). Early radio observations show that this galaxy is a weak radio source (Feretti & Giovannini 1980; Hummel 1980) with symmetric jets emanating from an unresolved core located at the optical center (Feretti et al. 1984).

The bright part of the X-ray emission is rather compact (1′), peaked on NGC 5322, and extends only to the south of the galaxy. There is a dip in the entropy map ∼1.′2 to the southwest from the center with no optical counterpart in DSS2 images. Due to the insufficient quality of the data we were able only to select six regions for the spectral analysis, precluding us from confirming the entropy dip. The enhancement in the pressure 3.′7 to the southeast of NGC 5322 is only marginally seen in the spectral analysis.

5.10. *NGC 5846, z* = 0.0063

This system reveals a number of ringlike structures in the image, which we identify with metallicity enhancements. No optical counterpart for this structure is seen in the DSS2 images, consistent with the idea of metallicity enhancements. Although an optical image reveals a small galaxy 0.′6 south of NGC 5846 (NGC 5846a, with a velocity difference of 500 km s^{-1}), it is not demarcated on the entropy map. This rules out a significant gas halo for this object, and so it should have in any case a negligible impact on the X-ray appearance.

The two-dimensional spectral mapping of the properties of the X-ray emission from NGC 5846 is done at the effective 6–10 kpc resolution, within the central 50 kpc. As the spectroscopic analysis shows (see Fig. 9), entropy, pressure, temperature, and iron abundance all appear relaxed, with only a slight displacement between the central peak and the center of the large-scale emission. The large-scale elongation of the entropy is confirmed and an associated elongation in the high-element abundance zone is found. In addition, some disturbance in the pressure map is observed in the core. Given the long timescale for the entropy disturbance to relax, it is not surprising that the associated radio activity is not observed. The presence of an AGN in NGC 5846 is supported by the detection of a central radio point source in the NRAO VLA Sky Survey (Becker et al. 1995). There is a zone of high Fe abundance 2′ to the northeast from the center (*shown in red*, Fig. 8), on the level of 0.75 ± 0.07 solar, compared to 0.50 ± 0.05 detected at a similar distance from the center, which is a base of our claim on metallicity variations. Patches of higher abundance (*shown in white*, Fig. 8) correspond to a 1.0 ± 0.3 values and are of marginal significance. Another possibility is that the structures seen in NGC 5846 are sound waves, as have recently been reported for the Perseus cluster (Fabian et al. 2003).

5.11. *NGC 7582, z* = 0.0054

The ∼5′ extent of the X-ray emission of NGC 7582 is shown in Figure 5. Two other galaxies, NGC 7590 and NGC 7599 (not shown in Fig. 5), also reveal extended X-ray emission on the scales of 1′–2′, each one centered on a galaxy. Our study confirms the lack of diffuse X-ray emission from this group reported by Mulchaey & Zabludoff (1998) based on the *ROSAT* data. NGC 7582 is a well-studied Seyfert 2 galaxy. Its hard (2–10 keV) X-ray emission has been detected in many X-ray surveys (Ward et al. 1978), and the X-ray spectrum of this AGN is complex (see Turner et al. 2000). Detailed spectroscopic analysis shows a presence of emission from the AGN and complex diffuse emission from the bright spiral galaxy (NGC 7582). Since the origin of the emission from the spiral galaxy is likely to be a mixture of emission from hot gas, point sources, and supernova remnants, which is quite different from the rest of the sample, we omit this system from further analysis.

In Koribalski (1996) the H I image of the NGC 7582 group was presented. A comparison shows that the X-ray emission is embedded within the Hα, and that the shape of the X-ray emission is determined by the star formation processes, as opposed to the case in which the hot gas fills the potential of the galaxy.

6. SUMMARY AND CONCLUSIONS

We performed an innovative two-dimensional analysis of the IGM properties in a representative sample of low-z groups of galaxies. We have well sampled the transition region between the regular groups and the X-ray faint groups and also have two examples of strong AGN feedback.

The properties of the hot gas in the X-ray-faint groups are studied for the first time at radii reaching $0.3r_{500}$. The properties of the hot gas in NGC 5322 and NGC 3923 deviate from the relations derived using brighter groups and clusters even at largest radii. These faint systems having higher entropy and lower pressure than expected. Our findings suggest that the X-ray-emitting gas in roughly half of X-ray-faint groups (groups with bolometric $L_X < 10^{41}$ ergs s^{-1}) does not originate from infalling gas heated to X-ray temperatures but instead is a by-product of the galaxy-galaxy merger activity associated with the formation of an elliptical galaxy. In fact, we note a similarity in the properties of the X-ray-faint groups studied here and the X-ray appearance of the postmerger galaxies.

Four other X-ray-faint groups, IC 1459, NGC 2300, NGC 4168, and NGC 4261, exhibit typical group IGM properties outside $0.2r_{500}$, and we consider them as regular groups. One such group, NGC 4261, also reveals AGN activity, and our study reveals faint X-ray cavities, filled with relativistic plasma, extending to a similar distance from the center. These are also reported in Croston et al. (2005), confirming their conclusion that AGN activity has a substantial impact on the state of the gas at the central part of groups.

Examination of the structure in the gas of three groups reveals fluctuations in the entropy and pressure on a typically 10%–30% and metallicity on the 30%–50% level. The larger scatter in the metallicity of the gas within the group, compared to its entropy, suggests a diversity in the origin of the gas in the core and supports the work on using the metallicity as a tracer of the formation of IGM. However, the use of metallicity measurements is currently limited to a small number of systems, due to requirement of a large number of detected counts in each region. In our study such analysis is only possible for NGC 4636, NGC 5044, and NGC 5846.[7]

The paper is based on observations obtained with *XMM-Newton*, a European Space Agency (ESA) science mission with instruments and contributions directly funded by ESA Member States and the USA (NASA). The *XMM-Newton* project is supported by the Bundesministerium für Bildung und Forschung/Deutsches Zentrum für Luft- und Raumfahrt (BMFT/DLR),

[7] Two-dimensional information released at http://www.mpe.mpg.de/2dXGS.

the Max Planck Society and the Heidenhain-Stiftung, and also by PPARC, CEA, CNES, and ASI. The authors thank an anonymous referee for an insightful report, which led to substantial improvements in the quality of presented material. A. F. thanks Joe Mohr, Stefano Borgani, Trevor Ponman, and Mark Henriksen for useful discussions. A. F. thanks Steve Helsdon for his help in the regression analysis. A. F. acknowledges support from BMBF/DLR under grant 50 OR 0207, MPG and partial support from NASA grant NNG04GF686. A. F. and M. Z. thank the Joint Astrophysical Center of the University of Maryland, Baltimore County for hospitality during their visit. D. S. D. acknowledges partial support for this project from NASA grant NAG5-12739. J. S. M. acknowledges partial support for this program from NASA grant NNG04GC846.

REFERENCES

Anders, E., & Grevesse, N. 1989, Geochim. Cosmochim. Acta, 53, 197
Becker, R. H., White, R. L., & Helfand, D. J. 1995, ApJ, 450, 559
Bender, R., Burstein, D., & Faber, S. M. 1992, ApJ, 399, 462
Biviano, A., & Katgert, P. 2004, A&A, 424, 779
Borgani, S., Finoguenov, A., Kay, S. T., Ponman, T. J., Springel, V., Tozzi, P., & Voit, G. M. 2005, MNRAS, 361, 233
Borgani, S., et al. 2004, MNRAS, 348, 1078
Briel, U. G., Finoguenov, A., & Henry, J. P. 2004, A&A, 426, 1
Buote, D. A., & Canizares, C. R. 1998, MNRAS, 298, 811
Buote, D. A., & Fabian, A. C. 1998, MNRAS, 296, 977
Burkert, A., & Naab, T. 2004, Coevolution of Black Holes and Galaxies, ed. L. C. Ho (Cambridge: Cambridge Univ. Press), 422
Churazov, E., Brüggen, M., Kaiser, C. R., Böhringer, H., & Forman, W. 2001, ApJ, 554, 261
Croston, J. H., Hardcastle, M. J., & Birkinshaw, M. 2005, MNRAS, 357, 279
David, L. P., Jones, C., Forman, W., & Daines, S. 1994, ApJ, 428, 544
Davies, R. L., et al. 1987, ApJS, 64, 581
Davis, D. S., Mulchaey, J. S., Mushotzky, R. F., & Burstein, D. 1996, ApJ, 460, 601
Dekel, A., Stoehr, F., Mamon, G. A., Cox, T. J., Novak, G. S., & Primack, J. R. 2005, Nature, 437, 707
de Vaucouleurs, G., et al. 1991, Third Reference Catalogue of Bright Galaxies (New York: Springer) (RC3)
Dolag, K., Vazza, F., Brunetti, G., & Tormen, G. 2005, MNRAS, 364, 753
Dos Santos, S., & Doré, O. 2002, A&A, 383, 450
Evrard, A. E., & Henry, J. P. 1991, ApJ, 383, 95
Fabbiano, G., et al. 2003, ApJ, 588, 175
Fabian, A. C., Sanders, J. S., Allen, S. W., Crawford, C. S., Iwasawa, K., Johnstone, R. M., Schmidt, R. W., & Taylor, G. B. 2003, MNRAS, 344, L43
Feretti, L., & Giovannini, G. 1980, A&A, 92, 296
Feretti, L., Giovannini, G., Hummel, E., & Kotanyi, C. G. 1984, A&A, 137, 362
Finoguenov, A., Böhringer, H., Osmond, J. P. F., Ponman, T. J., Sanderson, A. J. R., Zhang, Y.-Y., & Zimer, M. 2005, Adv. Space Sci., 36, 622
Finoguenov, A., Briel, U. G., & Henry, J. P. 2003a, A&A, 410, 777
Finoguenov, A., Burkert, A., Böhringer, H. 2003b, ApJ, 594, 136
Finoguenov, A., Henriksen, M. J., Briel, U. G., de Plaa, J., & Kaastra, J. S. 2004a, ApJ, 611, 811
Finoguenov, A., & Jones, C. 2000, ApJ, 539, 603
———. 2001, ApJ, 547, L107
Finoguenov, A., Jones, C., Böhringer, H., & Ponman, T. J. 2002, ApJ, 578, 74
Finoguenov, A., Jones, C., Forman, W., & David, L. 1999, ApJ, 514, 844
Finoguenov, A., & Miniati, F. 2004, A&A, 418, L21
Finoguenov, A., Pietsch, W. N., Aschenbach, B. R., & Miniati, F. 2004b, A&A, 415, 415
Finoguenov, A., & Ponman, T. J. 1999, MNRAS, 305, 325
Finoguenov, A., Ponman, T. J., Osmond, J. P. F., & Zimer, M. 2006, MNRAS, submitted
Finoguenov, A., Reiprich, T., Böhringer, H. 2001, A&A, 368, 749
Finoguenov, A., et al. 2004c, A&A, 419, 47
Forman, W., Jones, C., & Tucker, W. H. 1985, ApJ, 293, 102
Freyberg, M. J., et al. 2004, Proc. SPIE, 5165, 112
Garcia, A. M. 1993, A&AS, 100, 47
Geller, M. J., & Huchra, J. P. 1983, ApJS, 52, 61
Gliozzi, M., Sambruna, R. M., & Brandt, W. N. 2003, A&A, 408, 949
Gruendl, R. A., Vogel, S. N., Davis, D. S., & Mulchaey, J. S. 1993, ApJ, 413, L81
Helsdon, S. F., & Ponman, T. J. 2000, MNRAS, 319, 933
Henry, J. P., Finoguenov, A., & Briel, U. G. 2004, ApJ, 615, 181
Hickson, P. 1982, ApJ, 255, 382
Huchra, J. P., & Geller, M. J. 1982, ApJ, 257, 423
Hummel, E. 1980, A&AS, 41, 151
Hummel, E., & Beck, R. 1995, A&A, 303, 691
Hwang, U., Mushotzky, R. F., Burns, J. O., Fukazawa, Y., & White, R. A. 1999, ApJ, 516, 604
Jansen, F., et al. 2001, A&A, 365, L1
Jones, C., et al. 2002, ApJ, 567, L115
Kaiser, N. 1986, MNRAS, 222, 323
———. 1991, ApJ, 383, 104
King, I. R. 1978, ApJ, 222, 1
Kodama, T., Smail, I., Nakata, F., Okamura, S., & Bower, R. G. 2001, ApJ, 562, L9
Koprolin, W., & Zeilinger, W. W. 2000, A&AS, 145, 71
Koribalski, B. 1996, in ASP Conf. Ser. 106, The Minnesota Lectures on Extragalactic Neutral Hydrogen, ed. E. D. Skillman (San Francisco: ASP), 238
Mahdavi, A., Böhringer, H., Geller, M. J., & Ramella, M. 2000, ApJ, 534, 114
Mahdavi, A., Finoguenov, A., Böhringer, H., Geller, M. J., & Henry, J. P. 2005, ApJ, 622, 187
Maia, M. A. G., da Costa, L. M., & Latham, D. W. 1989, ApJS, 69, 809
Malin, D. F., & Carter, D. 1983, ApJ, 274, 534
Markevitch, M., Gonzalez, A. H., David, L., Vikhilin, A., Murray, S., Forman, W., Jones, C., & Tucker, W. 2002, ApJ, 567, L27
Mathews, W. G., Faltenbacher, A., Brighenti, F., & Buote, D. A. 2005, ApJ, 634, L137
Matsumoto, H., et al. 1997, ApJ, 482, 133
Matsushita, K. 2001, ApJ, 547, 693
Matsushita, K., Makishima, K., Ikebe, Y., Rokutanda, E., Yamasaki, N., & Ohashi, T. 1998, ApJ, 499, L13
Mazzotta, P., Fusco-Femiano, R., & Vikhlinin, A. 2002, ApJ, 569, L31
McNamara, B. R., Wise, M. W., Nulsen, P. E. J., David, L. P., & Carilli, C. L. 2001, ApJ, 562, L149
Metzler, C. A., & Evrard, A. E. 1994, ApJ, 437, 564
Michard, R. 1999, A&AS, 137, 245
Mulchaey, J. S. 2000, ARA&A, 38, 289
Mulchaey, J. S., Davis, D. S., Mushotzky, R. F., & Burstein, D. 1993, ApJ, 404, L9
———. 1996, ApJ, 456, 80
———. 2003, ApJS, 145, 39
Mulchaey, J. S., & Zabludoff, A. I. 1998, ApJ, 496, 73
———. 1999, ApJ, 514, 133
Nolthenius, R. 1993, ApJS, 85, 1
Osmond, J. P. F., & Ponman, T. J. 2004, MNRAS, 350, 1511
Ostriker, J. P., Lubin, L. M., & Hernquist, L. 1995, ApJ, 444, L61
Pedersen, K., Rasmussen, J., Sommer-Larsen, J., Toft, S., Benson, A. J., & Bower, R. G. 2006, NewA, 11, 465
Ponman, T. J., & Bertram, D. 1993, Nature, 363, 51
Ponman, T. J., Bourner, P. D. J., Ebeling, H., Böhringer, H. 1996, MNRAS, 283, 690
Ponman, T. J., Sanderson, A. J. R., & Finoguenov, A. 2003, MNRAS, 343, 331
Pratt, G. W., & Arnaud, M. 2003, A&A, 408, 1
Read, A. M., & Ponman, T. J. 1998, MNRAS, 297, 143
Reiprich, T. H., & Böhringer, H. 2002, ApJ, 567, 716
Ricker, P. M., & Sarazin, C. L. 2001, ApJ, 561, 621
Romanowsky, A. J., et al. 2003, Science, 301, 1696
Sato, S., & Tawara, Y. 1999, ApJ, 514, 765
Schindler, S. 2004, Ap&SS, 289, 419
Schuecker, P., Finoguenov, A., Miniati, F., Böhringer, H., & Briel, U. G. 2004, A&A, 426, 387
Stanger, V. J., & Warwick, R. S. 1986, MNRAS, 220, 363
Tamura, T., et al. 2001, A&A, 365, L87
Tittley, E. R., & Henriksen, M. 2005, ApJ, 618, 227
Tonry, J. L., Dressler, A., Blakeslee, J. P., Ajhar, E. A., Fletcher, A. B., Luppino, G. A., Metzger, M. R., & Moore, C. B. 2001, ApJ, 546, 681
Trinchieri, G., Kim, D.-W., Fabbiano, G., & Canizares, C. R. C. 1994, ApJ, 428, 555
Trinchieri, G., Sulentic, J., Breitschwerdt, D., & Pietsch, W. 2003, A&A, 401, 173
Turner, T. J., et al. 2000, ApJ, 531, 245
Vikhlinin, A., Markevitch, M., & Murray, S. S. 2001, ApJ, 551, 160
Vikhlinin, A., McNamara, B. R., Hornstrup, A., Quintana, H., Forman, W., Jones, C., & Way, M. 1999, ApJ, 520, L1
Vikhlinin, A., et al. 1998, ApJ, 502, 558
Voit, G. M., Balogh, M. L., Bower, R. G., Lacey, C. G., & Bryan, G. L. 2003, ApJ, 593, 272
Voit, G. M., & Ponman, T. J. 2003, ApJ, 594, L75
Ward, M. J., et al. 1978, ApJ, 223, 788
Zhang, Y.-Y., et al. 2004, A&A, 413, 49